

Iterative approaches to the self-consistent nuclear energy density functional problem.

Heavy ball dynamics and potential preconditioning.

W. Ryssens^{1,2}, M. Bender² and P.-H. Heenen³

¹ Center for Theoretical Physics, Sloane Physics Laboratory, Yale University, New Haven, CT 06520, USA.

² IPNL, Université de Lyon, Université Lyon 1, CNRS/IN2P3, F-69622 Villeurbanne, France .

³ PNTPM, CP229, Université Libre de Bruxelles, B-1050 Bruxelles, Belgium

the date of receipt and acceptance should be inserted later

Abstract. Large-scale applications of energy density functional (EDF) methods depend on fast and reliable algorithms to solve the associated non-linear self-consistency problem. When dealing with large single-particle variational spaces, existing solvers can become very slow, and their performance dependent on manual fine-tuning of numerical parameters. In addition, convergence can sensitively depend on particularities of the EDF's parametrisation under consideration. Using the widely-used Skyrme EDF as an example, we investigate the impact of the parametrisation of the EDF, both in terms of the operator structures present and the size of coupling constants, on the convergence of numerical solvers. We focus on two aspects of the self-consistency cycle, which are the diagonalisation of a fixed single-particle Hamiltonian on one hand and the evolution of the mean-field densities and potentials on the other. Throughout the article we use a coordinate-space representation, for which the behaviour of algorithms can be straightforwardly analysed. We propose two algorithmic improvements that are easily implementable in existing solvers, heavy-ball dynamics and potential preconditioning. We demonstrate that these methods can be made virtually parameter-free, requiring no manual fine-tuning to achieve near-optimal performance except for isolated cases. The combination of both methods decreases substantially the CPU time required to obtain converged results. The improvements are illustrated for the MOCCa code that solves the self-consistent HFB problem in a 3d coordinate space representation for parametrisations of the standard Skyrme EDF at next-to-leading order in gradients and its extension to next-to-next-to-leading order.

PACS. XX.XX.XX No PACS code given

1 Introduction

Many-body techniques based on energy density functionals (EDFs) offer a microscopic description of both ground-state and excited-state properties of atomic nuclei [1]. These methods have in common that the total binding energy is calculated from a functional of one-body densities that are constructed from auxiliary product states. On the most basic level, the self-consistent Hartree-Fock (HF), HF+BCS, or Hartree-Fock-Bogoliubov (HFB) equations are solved self-consistently to determine a product state whose densities minimise the total binding energy for a given EDF. On a more advanced level, correlations beyond the mean field are described as either a superposition of particle-hole excitations on top of such a reference state, or by mixing different reference states constructed with some systematically varied auxiliary conditions.

Over time, many different implementations have been set up, differing in their choice of numerical representation and in the nature of the EDF. Compared with other micro-

scopic methods, the computational cost of self-consistent mean-field methods scales rather favourably with system size, rendering the entirety of the nuclear chart accessible. The self-consistent equations present a nonlinear optimization problem, requiring iterative techniques to obtain their solution. Considering that every iteration requires the (approximate) diagonalisation of either a single-particle Hamiltonian or a quasiparticle Hamiltonian, computational requirements can nevertheless be substantial when employing large single-particle bases. As a result, computational resource requirements can still become a limiting factor, especially when aiming at systematic calculations across large sets of nuclei.

Large single-particle bases arise naturally in coordinate space approaches. Coordinate space approaches have the attractive feature that they offer easily controllable numerical accuracy, in both infrared and ultraviolet cutoffs, and this independently of the nuclear configuration [2]. For an harmonic oscillator (HO) basis, the other widely-used choice, control of convergence is much more delicate [3].

However, in full 3d geometry already modest choices of spatial discretization lead to matrices whose storage exceeds by far the typical memory capacity offered by the latest high-performance computing facilities. Fortunately, for many applications one can avoid dealing with full matrices, as one is only interested in a limited set of single-particle states with the lowest energy.

In terms of numerical cost, a coordinate-space representation is particularly competitive for EDFs that yield a local mean-field Hamiltonian. The non-relativistic Skyrme EDF is arguably the most widely one used among these. In this case the structure of the EDF is motivated by the expectation value of contact interactions with gradients and is built out of products of local densities and currents with internal and external derivatives. Significant efforts have been made to push the adjustment of its parameters such that there are fits that provide an overall high-quality description of certain classes of observables [4,5]. In the course of these studies, however, it has become clear that it is unlikely that any further significant improvement can be made within the standard form of the Skyrme EDF. This, in turn, motivates the ongoing study of its systematic extension.

The standard form of the Skyrme EDF includes terms up to second order in gradients, which in present terminology is called next-to-leading order (NLO). A possible and already explored way to extend it is to add higher-order bilinear gradient terms with four (next-to-next-to-leading order, N2LO) and six (N3LO) gradients [6,7,8]. Already the first exploratory test calculations with our codes involving such terms have indicated that widely-used algorithms for solving the self-consistent problem for standard Skyrme EDFs can fail to converge efficiently for these extended functionals, as we will discuss below.

The aim of this paper is to analyse the origin of the differences of behaviour between the parametrisations and to single out which terms of the EDFs govern the achievable convergence rate. We will then show how to improve the convergence properties of mean-field calculations, with two main requirements: to decrease the computing time and to set up algorithms whose convergence does not require a case-by-case fine tuning of numerical parameters that renders systematic calculations tedious. We focus on two aspects of the solution of the self-consistent mean-field equations in coordinate space. The first one is the diagonalisation of a given fixed mean-field Hamiltonian. We will call this part of the calculation the *diagonalisation* subproblem. It is usually achieved with some variant of the gradient-descent method in which a limited set of single-particle wave functions are evolved until they converge to the eigenstates with the lowest eigenvalues [9, 10]. The second aspect is the evolution of the potentials entering the mean-field Hamiltonian, which depend on one-body densities constructed from the eigenstates of the mean-field Hamiltonian. We will refer to this part as the *self-consistent field* (SCF) subproblem. This second aspect of the self-consistent problem is often limited to a linear mixing of densities between two iterations. Two further subproblems have to be dealt with when solving

the mean-field equations: we will address the treatment of constraints during the SCF iterations in a second paper, while our present strategy to treat the pairing subproblem is briefly evoked in appendix A.

We propose two improvements that are easy to implement in existing solvers: *Heavy ball dynamics* for the diagonalisation of the mean-field Hamiltonian and *potential preconditioning* for the evolution of the potential. These proposed improvements were implemented and tested with the MOCCa code [11]. This mean-field solver is based on the same principles as the public EV8 code [10,12], but supersedes its functionalities by offering a wide range of symmetry options that give access to a larger range of applications.

While significant parts of the discussion are tailored to the Skyrme EDF equations in coordinate-space representation, the algorithms we discuss and the proposed improvements do neither depend on the choice of EDF nor on the choice of numerical representation and can also be easily adapted to other frameworks. Indeed, some groups also developed Cartesian 3d coordinate-space HF solvers that can handle the non-local exchange part of the finite-range Gogny interaction [13,14]. The additional integrals, however, substantially increase the computational cost, as would including pairing correlations. Therefore, systematic HFB calculations with this interaction are habitually performed in a HO-basis representation. The matrix elements of Gaussian forces then take a separable form which allows for very reasonable precision at moderate computational cost. Such representation in general favours iteration algorithms that evolve directly the Thouless matrix representing the HFB state [15,16,17] instead of the strategy we will discuss below. For effective Hamiltonians that cannot be easily mapped on Gaussians, however, the advantages of using a HO basis are less evident. For example, the 3d HF solver designed for the realistic low-momentum interaction V_{lowk} described in Ref. [18] uses the same plane-wave basis that also underlies Cartesian coordinate-space representations [2].

This paper is organised as follows. In Section 2 we introduce the general form of the Skyrme functional used here as well as the self-consistent problem. We study the diagonalisation of the single-particle Hamiltonian in Section 3 and the iterative treatment of mean-field densities and mean-field potentials in Section 4. Finally, numerical tests of the proposed improvements are presented in Section 5.

2 The self-consistent Skyrme-HFB problem on a coordinate space mesh

2.1 The SCF equations with the two-basis method

The energy of the nuclear configuration is determined by an energy functional that consists of five terms [1,19]

$$E_{\text{tot}} = E_{\text{kin}} + E_{\text{Sk}} + E_{\text{Coul}} + E_{\text{cm}} + E_{\text{pair}}. \quad (1)$$

These are the kinetic energy E_{kin} , the Skyrme EDF E_{Sk} modelling the strong interaction between nucleons in the

particle-hole channel, the Coulomb energy E_{Coul} resulting from the electromagnetic repulsion between protons, a centre-of-mass correction E_{cm} and a pairing EDF modelling the strong interaction between nucleons of the same species in the particle-particle channel. These five terms are provided by functionals of normal and anomalous one-body densities that are calculated from an auxiliary many-body product state.

Depending on the treatment of pairing correlations, this state is either a Slater determinant (HF) or a Bogoliubov quasiparticle vacuum (HF+BCS and HFB), which is represented in an underlying basis of single-particle orbitals $\phi_j(\mathbf{r}) = \langle \mathbf{r} | a_j^\dagger | - \rangle$ of dimension N_b . Here and in the following, except when needed, we do not specify the isospin labels that introduce a block structure into all matrices in the single-particle basis.

Within a given single-particle basis, the single-particle Hamiltonian \hat{h} and the pairing tensor Δ are defined by the functional derivatives of the EDF with respect to the normal density matrix ρ and the anomalous density matrix κ [20]

$$h_{ij} = \frac{\delta E}{\delta \rho_{ji}} = h_{ji}^*, \quad (2)$$

$$\Delta_{ij} = \frac{\partial E}{\delta \kappa_{ij}^*} = -\Delta_{ji}. \quad (3)$$

Together they form the HFB quasiparticle Hamiltonian \mathcal{H}

$$\mathcal{H} = \begin{pmatrix} h - \lambda & \Delta \\ -\Delta^* & -h^* + \lambda \end{pmatrix}, \quad (4)$$

where the Fermi energy λ is a Lagrange multiplier whose value has to be adjusted to fix the average number of particles to the targeted number of neutrons (N) or protons (Z), respectively. The diagonalisation of \mathcal{H} yields a set of eigenvectors $(U_\mu V_\mu)^T$

$$\mathcal{H} \begin{pmatrix} U_\mu \\ V_\mu \end{pmatrix} = E_\mu^{\text{qp}} \begin{pmatrix} U_\mu \\ V_\mu \end{pmatrix} \quad (5)$$

that represent the quasi-particle wave functions with quasi-particle energy E_μ^{qp} , and which we call *HFB basis*.

One can solve the problem by diagonalising \mathcal{H} in the full space of dimension $2N_b$, which is for instance done in [21]. When N_b is large, however, it becomes challenging to store the relevant matrices, let alone diagonalise them. The problem can remain feasible however, if one introduces a cutoff of the pairing interaction, reducing the number of quasiparticles to those that meaningfully contribute to the auxiliary state.

The two-basis method, first introduced in [22], offers a straightforward way to introduce such a cutoff. The method relies on the construction of the single-particle states that diagonalise \hat{h}

$$\hat{h}|\psi_j\rangle = \epsilon_j |\psi_j\rangle \quad (6)$$

that is called the HF basis. Within this basis, a pairing cutoff can easily be defined as a function of the Fermi

energy λ and the diagonal matrix elements of \hat{h} . This effectively limits the relevant space of the HFB problem to a small number of states in the HF basis. We denote the effective size of the HF basis by Ω . The numerical burden is then completely shifted to the construction of the HF basis in the full single-particle space.

For this reason, we focus on the self-consistent construction of the HF basis in the following. While an appropriate algorithm for the partial diagonalisation of \mathcal{H} is an essential ingredient of a successful calculation, we assume that a reliable and fast implementation is available. In practice, the only output of such algorithm that is required for the purpose of our study is the set of matrix elements ρ_{ij} and κ_{ij} in the HF basis. These can then be used to construct the mean-field densities as defined in Section 2.3.

2.2 Representation in 3D coordinate space

While leaving the discussion as general as possible, we assume a 3d representation in coordinate space. For the spatial discretization, we choose an equidistant Cartesian mesh with $N_m = N_x \times N_y \times N_z$ coordinate space coordinates \mathbf{r}_{ijk} , where the total number of points is determined by the distance between the discretization points and the volume of the box. Any function $f(\mathbf{r})$ on the mesh is then represented by its values at the discretization points

$$f(\mathbf{r}) \rightarrow f(x_i, y_j, z_k) = f(\mathbf{r}_{ijk}) \equiv f_{ijk}. \quad (7)$$

In particular, the single-particle wave functions $|\psi\rangle$ are represented as spinors $\psi(\mathbf{r})$

$$|\psi\rangle \rightarrow \psi(\mathbf{r}_{ijk}) = \begin{pmatrix} \psi(\mathbf{r}_{ijk}, \sigma = +) \\ \psi(\mathbf{r}_{ijk}, \sigma = -) \end{pmatrix}, \quad (8)$$

meaning that for each nucleon species one can construct $2N_m$ different single-particle wave functions on the mesh. A typical choice is $N_X = N_Y = N_Z = 40$ [2], which implies a basis of 128000 single-particle wave functions for each nucleon species.

The integral of an arbitrary function over the volume of the box is given by the N_m -point rectangular rule [2]

$$\int_V d^3r f(r) \rightarrow \sum_{ijk} f_{ijk}. \quad (9)$$

The calculation of the derivatives of functions is equivalent to a matrix multiplication. In the case of the Laplacian of a function $f(\mathbf{r})$ at the point \mathbf{r}_{ijk} , one has to calculate

$$\begin{aligned} [\Delta f](\mathbf{r}_{ijk}) &= [(\partial_x^2 + \partial_y^2 + \partial_z^2) f](\mathbf{r}_{ijk}) \\ &= \left(\sum_{p=1}^{N_x} D_{ip}^{(2)} f_{pjk} + \sum_{q=1}^{N_y} D_{jq}^{(2)} f_{iqk} + \sum_{r=1}^{N_z} D_{kr}^{(2)} f_{ijr} \right), \end{aligned} \quad (10)$$

where the matrices $D^{(2)}$ represent the second derivative in a given Cartesian direction. There are several possible choices for their form. We use Lagrange mesh derivatives [2, 23], for which the $D^{(2)}$ are full matrices, as they

provide very accurate results already for very coarse meshes, i.e. a modest number of mesh points N_m . The Lagrange derivatives have the clear advantages that partial integrations are exact up to machine precision, and that higher-order derivative matrices can be calculated as products of matrices of first-order derivatives. Together with the quadrature rule of Eq. (9), they implicitly define an underlying basis of plane waves in a box [2], such that this special case of coordinate-space representation can be unambiguously treated with the standard techniques of linear algebra.

A widely-used alternative are finite difference formulas. These correspond to sparse matrices $D^{(2)}$ that can be very efficiently multiplied, but on a given mesh are much less accurate than Lagrange-mesh derivatives [2]. The reasons are that partial derivatives are not exact and that higher-order derivative matrices are not numerically equivalent to repeated applications of the first-order derivative matrix. This can be compensated for by increasing the number of mesh points in for a given volume. For NLO Skyrme EDFs, there is also the time-tested possibility to arrive at very satisfying results by solving the HFB equations using finite-difference formulas and to recalculate all observables with Lagrange derivatives after convergence [2]. For terms with four derivatives in the Skyrme N2LO EDF, however, this procedure becomes less reliable.

2.3 The Skyrme functional

We discuss in detail the two terms from Eq. (1) that are relevant for our discussion: the kinetic energy E_{kin} and the Skyrme energy E_{Sk} . For a discussion of the other terms, we refer to Ref. [12].

The Skyrme part E_{Sk} of the EDF is built out of local one-body densities. For the purpose of our discussion, it is sufficient to limit ourselves to the central and spin-orbit parts at NLO, for which we will analyse time-even and time-odd terms, and the time-even part of the N2LO functional with additional central terms as proposed in [8]. Further terms, such as tensor terms at NLO [24, 25, 26], additional density dependences of NLO terms [27], and three-body interactions up to NLO [28, 29] have been considered in the literature, but as far as the numerical solution of the self-consistent mean-field equations is concerned, these do not behave differently from the terms discussed here.

Densities. Assuming that all single-particle states either represent a neutron or a proton, the full one-body density matrix for the nucleon species $q = n, p$ in coordinate space can be split into a scalar and a vector in spin space [30]

$$\begin{aligned} \rho_q(\mathbf{r}\sigma, \mathbf{r}'\sigma') &= \sum_{jk} \rho_{kj} \psi_j^*(\mathbf{r}'\sigma') \psi_k(\mathbf{r}, \sigma) \\ &= \frac{1}{2} \rho_q(\mathbf{r}, \mathbf{r}') + \frac{1}{2} \langle \sigma' | \hat{\boldsymbol{\sigma}} | \sigma \rangle \cdot \mathbf{s}_q(\mathbf{r}, \mathbf{r}'), \end{aligned} \quad (11)$$

The ρ_{jk} are the elements of the density matrix determined by the solution of the HFB problem in the restricted set of Ω states of the HF basis.

The local mean-field densities used to define the Skyrme EDF at NLO in its form relevant for our discussion are

$$\rho_q(\mathbf{r}) = \rho_q(\mathbf{r}, \mathbf{r}') \Big|_{\mathbf{r}=\mathbf{r}'}, \quad (12a)$$

$$\tau_q(\mathbf{r}) = \nabla \cdot \nabla' \rho_q(\mathbf{r}, \mathbf{r}') \Big|_{\mathbf{r}=\mathbf{r}'}, \quad (12b)$$

$$J_{q,\mu\nu}(\mathbf{r}) = -\frac{i}{2} (\nabla_\mu - \nabla'_\mu) s_{q,\nu}(\mathbf{r}, \mathbf{r}') \Big|_{\mathbf{r}=\mathbf{r}'}, \quad (12c)$$

$$\mathbf{s}_q(\mathbf{r}) = \mathbf{s}_q(\mathbf{r}, \mathbf{r}') \Big|_{\mathbf{r}=\mathbf{r}'}, \quad (12d)$$

$$\mathbf{T}_q(\mathbf{r}) = \nabla \cdot \nabla' \mathbf{s}_q(\mathbf{r}, \mathbf{r}') \Big|_{\mathbf{r}=\mathbf{r}'}, \quad (12e)$$

$$\mathbf{j}_q(\mathbf{r}) = -\frac{i}{2} (\nabla_\mu - \nabla'_\mu) \rho_q(\mathbf{r}, \mathbf{r}') \Big|_{\mathbf{r}=\mathbf{r}'}. \quad (12f)$$

The local density $\rho_q(\mathbf{r})$, kinetic density $\tau_q(\mathbf{r})$ and spin-current tensor density $J_{q,\mu\nu}(\mathbf{r})$ are even under time-reversal, whereas the spin density $\mathbf{s}_q(\mathbf{r})$, kinetic spin density $\mathbf{T}_q(\mathbf{r})$ and current density $\mathbf{j}_q(\mathbf{r})$ are odd. As a consequence, the latter are zero when time-reversal invariance is imposed.

The N2LO Skyrme functional requires the introduction of additional local densities that either contain additional derivatives or have a more complicated tensor structure than the NLO densities. There are several possible choices [31]; we use here the convention of Ref. [8], where the densities that contribute in time-reversal-invariant systems are given by

$$\tau_{q,\mu\nu}(\mathbf{r}) = \nabla_\mu \nabla'_\nu \rho_q(\mathbf{r}, \mathbf{r}') \Big|_{\mathbf{r}=\mathbf{r}'}, \quad (13a)$$

$$K_{q,\mu\nu\kappa}(\mathbf{r}) = \nabla_\mu \nabla'_\nu s_{q,\kappa}(\mathbf{r}, \mathbf{r}') \Big|_{\mathbf{r}=\mathbf{r}'}, \quad (13b)$$

$$V_{q,\mu\nu}(\mathbf{r}) = -\frac{i}{2} (\nabla_\mu - \nabla'_\mu) (\nabla \cdot \nabla') s_{q,\nu}(\mathbf{r}, \mathbf{r}') \Big|_{\mathbf{r}=\mathbf{r}'}, \quad (13c)$$

$$Q_q(\mathbf{r}) = \Delta \Delta' \rho_q(\mathbf{r}, \mathbf{r}') \Big|_{\mathbf{r}=\mathbf{r}'}. \quad (13d)$$

The densities $Q_q(\mathbf{r})$ and $V_{q,\mu\nu}(\mathbf{r})$ are time-even, whereas $\tau_{q,\mu\nu}(\mathbf{r})$ and $K_{q,\mu\nu\kappa}(\mathbf{r})$ are neither time-even nor time-odd. Note that the NLO densities $\tau_q(\mathbf{r})$ and $\mathbf{T}_q(\mathbf{r})$ are contractions of the full tensor densities $\tau_{q,\mu\nu}(\mathbf{r})$ and $K_{q,\mu\nu\kappa}(\mathbf{r})$ needed for the N2LO functional.

The kinetic energy. The kinetic energy E_{kin} can be written as a functional of the local kinetic density $\tau_q(\mathbf{r})$ as

$$E_{\text{kin}} = \sum_{q=n,p} \int d^3r \frac{\hbar^2}{2m_q} \tau_q(\mathbf{r}), \quad (14)$$

where m_q is the mass of the nucleon species $q = n, p$.

The Skyrme energy. In what follows, we analyse the behaviour of time-even and time-odd terms at the NLO level on the one hand, and the behaviour of the time-even terms in an extended functional with N2LO terms on the other hand

$$E_{\text{Sk}}^{\text{N2LO}} = \int d^3r \left[\mathcal{E}_{\text{Sk},e}^{(0)}(\mathbf{r}) + \mathcal{E}_{\text{Sk},e}^{(2)}(\mathbf{r}) + \mathcal{E}_{\text{Sk},o}^{(0)}(\mathbf{r}) + \mathcal{E}_{\text{Sk},o}^{(2)}(\mathbf{r}) \right], \quad (15)$$

$$E_{\text{Sk},e}^{\text{N2LO}} = \int d^3r \left[\mathcal{E}_{\text{Sk},e}^{(0)}(\mathbf{r}) + \mathcal{E}_{\text{Sk},e}^{(2)}(\mathbf{r}) + \mathcal{E}_{\text{Sk},e}^{(4)}(\mathbf{r}) \right], \quad (16)$$

where the superscripts (0), (2), and (4) indicate the order in derivatives and the subscripts e and o if the terms are bilinear in time-even or time-odd local densities, respectively. The various energy densities up to NLO read

$$\mathcal{E}_{\text{Sk},e}^{(0)}(\mathbf{r}) = \sum_{t=0,1} \left[C_t^{\rho\rho} \rho_t^2(\mathbf{r}) + C_t^{\rho\rho\rho^\alpha} \rho_0^\alpha(\mathbf{r}) \rho_t^2(\mathbf{r}) \right], \quad (17)$$

$$\begin{aligned} \mathcal{E}_{\text{Sk},e}^{(2)}(\mathbf{r}) = & \sum_{t=0,1} \left[C_t^{\rho\tau} \rho_t(\mathbf{r}) \tau_t(\mathbf{r}) + C_t^{\rho\Delta\rho} \rho_t(\mathbf{r}) \Delta\rho_t(\mathbf{r}) \right. \\ & + C_t^{\rho\nabla\cdot J} \rho_t(\mathbf{r}) \nabla \cdot \mathbf{J}_t(\mathbf{r}) \\ & \left. - C_t^{sT} \sum_{\mu,\nu} J_{t,\mu\nu}(\mathbf{r}) J_{t,\mu\nu}(\mathbf{r}) \right], \quad (18) \end{aligned}$$

$$\mathcal{E}_{\text{Sk},o}^{(0)}(\mathbf{r}) = \sum_{t=0,1} \left[C_t^{ss} \mathbf{s}_t^2(\mathbf{r}) + C_t^{ss\rho^\alpha} \rho_0^\alpha(\mathbf{r}) \mathbf{s}_t^2(\mathbf{r}) \right], \quad (19)$$

$$\begin{aligned} \mathcal{E}_{\text{Sk},o}^{(2)}(\mathbf{r}) = & \sum_{t=0,1} \left[C_t^{sT} \mathbf{s}_t(\mathbf{r}) \cdot \mathbf{T}_t(\mathbf{r}) + C_t^{\Delta s} \mathbf{s}_t(\mathbf{r}) \cdot \Delta \mathbf{s}_t(\mathbf{r}) \right. \\ & \left. - C_t^{\rho\tau} \mathbf{j}_t^2(\mathbf{r}) + C_t^{\rho\nabla\cdot J} \mathbf{s}_t(\mathbf{r}) \cdot \nabla \times \mathbf{j}_t(\mathbf{r}) \right], \quad (20) \end{aligned}$$

where proton and neutron densities have been recoupled to isoscalar ($t = 0$) and isovector ($t = 1$) ones, for example $\rho_0(\mathbf{r}) = \rho_n(\mathbf{r}) + \rho_p(\mathbf{r})$ and $\rho_1(\mathbf{r}) = \rho_n(\mathbf{r}) - \rho_p(\mathbf{r})$. In the last term of Eq. (18) the summation is over Cartesian components of the tensor density, while the rank-1 contraction \mathbf{J}_q of the spin-current density $J_{q,\mu\nu}$ is given by [24]

$$J_{q,\mu}(\mathbf{r}) = \sum_{\nu\kappa} \epsilon_{\mu\nu\kappa} J_{q,\nu\kappa}(\mathbf{r}). \quad (21)$$

We have written Eqs. (18) and (20) with the usual convention that terms that have to be combined in order to ensure Galilean invariance of the EDF have the same coupling constant [26].

Similarly, the part of the N2LO extension of the Skyrme functional depending on time-even densities can be written as

$$\begin{aligned} \mathcal{E}_{\text{Sk},e}^{(4)}(\mathbf{r}) = & \sum_{t=0,1} \left[C_t^{\Delta\rho\Delta\rho} (\Delta\rho_t(\mathbf{r}))^2 + C_t^{\tau\tau} \tau_t^2(\mathbf{r}) \right. \\ & + C_t^{\rho Q} \rho_t(\mathbf{r}) Q_t(\mathbf{r}) + 2 C_t^{\tau\mu\nu\tau\mu\nu} \sum_{\mu,\nu} \tau_{t,\mu\nu}^2(\mathbf{r}) \\ & - 2 C_t^{\tau\nabla\nabla\rho} \sum_{\mu,\nu} \tau_{t,\mu\nu}(\mathbf{r}) \nabla_\mu \nabla_\nu \rho_t(\mathbf{r}) \\ & + 2 C_t^{KK} \sum_{\mu,\nu,\kappa} (K_{t,\mu\nu\kappa}(\mathbf{r}))^2 \\ & \left. - 2 C_t^{JV} \sum_{\mu,\nu} J_{t,\mu\nu}(\mathbf{r}) V_{t,\mu\nu}(\mathbf{r}) \right], \quad (22) \end{aligned}$$

where all sums are over Cartesian components of the tensors and where we have opted to label the coupling constants C_t for each term separately, even though many are identical to guarantee the Galilean invariance of the EDF [8].

The single-particle Hamiltonian. To simplify the notation, we introduce the density-vector \mathbf{R} as a helpful short-

hand for the set of mean-field densities. For the two cases we discuss below, it is given by

$$\mathbf{R}_q^{\text{NLO}} = (\rho_q, \tau_q, J_{q,\mu\nu}, \mathbf{s}_q, \mathbf{T}_q, \mathbf{j}_q), \quad (23)$$

$$\mathbf{R}_q^{\text{N2LO}} = (\rho_q, \tau_q, \mu\nu, J_{q,\mu\nu}, K_{q,\mu\nu\kappa}, V_{q,\mu\nu}, Q_q), \quad (24)$$

where we use the indices a, b, \dots to refer to the individual components of $\mathbf{R}_{q,a}(\mathbf{r})$, $q = n, p$.

With this density vector, the expression for the energy can be rewritten as $E_{\text{tot}}(\mathbf{R})$. The individual terms in the single-particle Hamiltonian are then obtained by rewriting the variation of the energy with respect to the full density matrix in Eq. (2) as the sum of variations with respect to the individual densities $\mathbf{R}_{q,a}(\mathbf{r})$ as

$$h_q(\mathbf{r}\sigma, \mathbf{r}'\sigma') = \sum_a \int d^3r'' \frac{\delta E}{\delta \mathbf{R}_{q,a}(\mathbf{r}'')} \frac{\delta \mathbf{R}_{q,a}(\mathbf{r}'')}{\delta \rho_q(\mathbf{r}'\sigma', \mathbf{r}\sigma)}. \quad (25)$$

The derivative of the energy with respect to the density $\mathbf{R}_{q,a}(\mathbf{r})$ can be identified as an associated mean-field potential $F_{q,a}(\mathbf{r})$

$$F_{q,a}(\mathbf{r}) \equiv \frac{\delta E}{\delta \mathbf{R}_{q,a}(\mathbf{r})} \quad (26)$$

that in general depends on the density vectors $\mathbf{R}_{p,a}(\mathbf{r})$ and $\mathbf{R}_{n,a}(\mathbf{r})$ of both nucleon species.

In analogous fashion, we introduce the potential-vector \mathbf{F} , which for the two types of EDF we consider here reads

$$\mathbf{F}_q^{\text{NLO}} = (\mathbf{F}_q^\rho, \mathbf{F}_q^\tau, \mathbf{F}_{q,\mu\nu}^J, \mathbf{F}_q^s, \mathbf{F}_q^T, \mathbf{F}_q^j), \quad (27)$$

$$\mathbf{F}_q^{\text{N2LO}} = (\mathbf{F}_q^\rho, \mathbf{F}_{q,\mu\nu}^\tau, \mathbf{F}_{q,\mu\nu}^J, \mathbf{F}_{q,\mu\nu\kappa}^K, \mathbf{F}_{q,\mu\nu}^V, \mathbf{F}_q^Q). \quad (28)$$

The corresponding single-particle Hamiltonians can then be written as a function of these potential-vectors

$$\begin{aligned} \hat{h}_q^{\text{NLO}}[\mathbf{F}] = & \mathbf{F}_q^\rho(\mathbf{r}) + \mathbf{F}_q^s(\mathbf{r}) \cdot \boldsymbol{\sigma} - i \mathbf{F}_q^j \cdot \nabla \\ & - i \sum_{\mu,\nu} \mathbf{F}_{q,\mu\nu}^J(\mathbf{r}) \nabla_\mu \sigma_\nu - \nabla \cdot \mathbf{F}_q^T(\mathbf{r}) \nabla \\ & - \sum_{\kappa} \nabla \cdot \mathbf{F}_{q\kappa}^T \nabla \sigma_\kappa, \quad (29) \end{aligned}$$

$$\begin{aligned} \hat{h}_q^{\text{N2LO}}[\mathbf{F}] = & \mathbf{F}_q^\rho(\mathbf{r}) + \mathbf{F}_q^s(\mathbf{r}) \cdot \boldsymbol{\sigma} - i \mathbf{F}_q^j \cdot \nabla \\ & - \frac{i}{2} \sum_{\mu,\nu} \left[\mathbf{F}_{q,\mu\nu}^J(\mathbf{r}) \nabla_\mu \sigma_\nu + \nabla_\mu \mathbf{F}_{q,\mu\nu}^J(\mathbf{r}) \sigma_\nu \right] \\ & - \sum_{\mu,\nu} \left[\nabla_\mu \mathbf{F}_{q,\mu\nu}^\tau(\mathbf{r}) \nabla_\nu + \sum_{\kappa} \nabla_\mu \mathbf{F}_{\mu\nu\kappa}^T \nabla_\nu \sigma_\kappa \right] \\ & + i \sum_{\mu,\nu,\kappa} \nabla_\kappa \mathbf{F}_{q,\mu\nu}^V \nabla_\nu \nabla_\mu \sigma_\kappa + \Delta \mathbf{F}_q^Q \Delta, \quad (30) \end{aligned}$$

where we have ordered the various terms according to the order of gradients that act on the single-particle wave functions, from lowest (0) to highest (4). The operator structure of the individual terms results from the second functional derivative in the chain rule in Eq. (25). We also simplified the single-particle Hamiltonians in Eqs. (29) and (30) by using that the gradients of certain potentials vanish for the EDFs used here. For more details on the

EDF at the NLO level, we refer the reader to [1,26]. A detailed discussion of the full EDF at N2LO level, including the time-odd terms, will be given elsewhere [31].

These equations show that the derivatives of the single-particle wave functions are needed at two different stages of the calculation, when summing up the local densities R_q , and when calculating the action of the single-particle Hamiltonian \hat{h}_q on the single-particle states. To minimise the computational cost, it is customary to calculate all necessary derivatives only once each time a new set of single-particle states has been determined during the iterative process and to store them for later use during the iteration.

The gradients contained in the kinetic and Skyrme terms of the EDF determine to a large extent the behaviour of the strategies employed for the diagonalisation subproblem and for the SCF iterations. They enter into these terms in two distinct ways: either as an *external gradient* acting on a local density, for example $\Delta\rho(\mathbf{r})$, or as an *internal gradient* that is contained within the definition of a local density, as for example in the definition of $\tau(\mathbf{r})$, Eq. (13a). Internal derivatives within the densities determine the operator structure of \hat{h}_q , whereas external derivatives contribute to the expressions for the potentials $F_q(\mathbf{r})$. As we discuss in what follows, the operator structure of the single-particle Hamiltonian (and hence internal derivatives) determines the convergence of the diagonalisation subproblem, whereas external derivatives of the densities $R_{q,a}(\mathbf{r})$ contribute to the expressions for the potentials $F_{q,a}(\mathbf{r})$.

2.4 The self-consistent problem

The single-particle Hamiltonian of the nucleon species q is a function of the vector F_q , which depends on the vectors of the densities R_p and R_n of protons and neutrons, which in turn are constructed from the single-particle wave functions. The equations to be solved are:

$$\hat{h}(\mathbf{F}[R(|\psi_1\rangle, |\psi_2\rangle, \dots)]) |\psi_j\rangle = \epsilon_j |\psi_j\rangle. \quad (31)$$

Since the single-particle Hamiltonian depends on its solution, the problem is highly non-linear and can only be solved by an iterative process. All quantities that depend on the iteration number i will be marked by a superscript (i) :

$$|\psi_j^{(i)}\rangle, R^{(i)}, F^{(i)}, h^{(i)}.$$

The usual strategy followed to solve the mean-field equations is composed of several separate, but linked, steps.

The first step is the (partial) diagonalisation of $\hat{h}^{(i)}$, to obtain a set of single-particle orbitals $|\psi_i^{(i+1)}\rangle$. With a fixed mean-field potential-vector F , this is a linear algebra problem. We call this the *diagonalisation* subproblem.

In order to obtain the matrix elements of ρ and κ , the second step is the restricted diagonalisation of the HFB Hamiltonian \mathcal{H} of Eq. (4). We call this the pairing subproblem, which is discussed briefly in Appendix A.

The third step is the evolution of the single-particle Hamiltonian from one iteration to the next. Suppose the single-particle Hamiltonian $h^{(i)}$ has been constructed in iteration (i) . Its eigenstates, which we label as $|\psi_j^{(i+1)}\rangle$, then provide the starting point for the next iteration.

The ensemble of these steps defines a map G^F on the space of F :

$$G^F : F^{(i)} \rightarrow G^F(F^{(i)}) = F_{|\psi}^{(i+1)}, \quad (32)$$

where $F_{|\psi}^{(i+1)}$ is calculated from the mean-field densities $R^{(i+1)}$ using the formulas presented in Section 2.3. Since the potentials F depend on the densities R , we can alternatively formulate this process as a map on the space of the densities

$$G^R : R^{(i)} \rightarrow G^R(R^{(i)}) = R_{|\psi}^{(i+1)}, \quad (33)$$

where this time the density $R_{|\psi}^{(i+1)}$ is calculated from the single-particle states $|\psi^{(i+1)}\rangle$ after diagonalisation of $h^{(i)}$.

Self-consistency is achieved when the potentials and densities get mapped onto themselves, meaning that

$$G^F(F^{(\infty)}) = F^{(\infty)}, \quad G^R(R^{(\infty)}) = R^{(\infty)}. \quad (34)$$

The evolution of the mean-field densities and potentials with the iterations should thus be aimed at finding the fixed points $F^{(\infty)}$ and $R^{(\infty)}$ of the maps G^R and G^F . We demonstrate in Section 4 that taking directly

$$F^{(i+1)} = F_{|\psi}^{(i+1)}, \quad R^{(i+1)} = R_{|\psi}^{(i+1)}, \quad (35)$$

does in general not lead to a stable iterative process. A more robust procedure to determine $F^{(i+1)}$ and $R^{(i+1)}$ from the potential and density vectors at iteration (i) is needed to achieve a stable iterative scheme. As already proposed in the introduction, we call the evolution of the potentials and densities the *self-consistent-field* (SCF) iteration, which is the frequently used terminology in atomic physics [32].

It is customary to introduce constraints on the expectation values of specific one-body operators into the mean-field equations, specifying for instance the multipole moments of the nuclear density. In practice, such constraints add terms to the single-particle Hamiltonian but otherwise affect neither the diagonalisation nor the SCF subproblems. We postpone the discussion of strategies how to efficiently treat constraints in the context of the algorithms discussed here to a future publication.

Since the mean-field Hamiltonian $\hat{h}^{(i)}$ changes at each iteration, it is not necessary to perform an accurate diagonalisation at each SCF iteration. The densities and potentials can be constructed from approximate eigenstates of $\hat{h}^{(i)}$. In electronic structure physics, such procedure reduces the CPU time by an order of magnitude [33]. In the case of a 3d coordinate space representation, this is particularly advantageous as the cost of diagonalising \hat{h} dwarfs the cost of updating the densities and potentials.

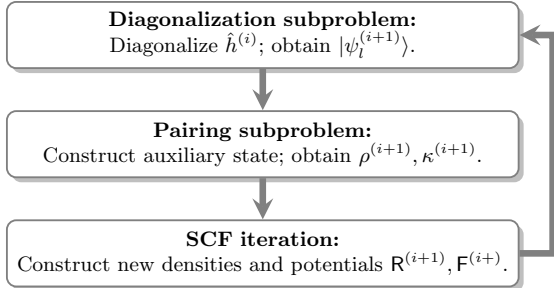


Fig. 1. Schematic diagram of the division into subproblems of the general solution strategy for the self-consistent problem.

The division of the resolution of the mean-field equations in different steps is illustrated in Fig. 1. While all steps in this figure are coupled in a practical implementation, we will discuss them separately in the next sections.

3 The diagonalisation subproblem

3.1 Iterative diagonalisation

Given a single-particle Hamiltonian $\hat{h}^{(i)}$, generated by the potentials $\mathbf{F}^{(i)}$, we are looking for its exact eigenstates $|\psi_\ell^{\text{ex}}\rangle$ and its eigenvalues $\epsilon_\ell^{\text{ex}}$

$$\hat{h}^{(i)}|\psi_\ell^{\text{ex}}\rangle = \epsilon_\ell^{\text{ex}}|\psi_\ell^{\text{ex}}\rangle. \quad (36)$$

To exclude the trivial null solution and to enforce that the single-particle states are orthonormalised, the numerical solution of Eq. (36) has to be supplemented by constraints on orthonormality

$$\langle\psi_k^{\text{ex}}|\psi_\ell^{\text{ex}}\rangle = \delta_{k\ell}. \quad (37)$$

In practice, Eq. (36) is a matrix equation whose dimension is equal to the size of the basis used to solve the problem. If this dimension is small enough, the problem can be solved by a direct diagonalisation using standard library routines. Several codes using an expansion in a HO basis employ this strategy [34,35]. This is also feasible in coordinate space representation when 1d spherical symmetry is assumed [36]. We are interested in the following in cases where the dimension of the basis is too large to permit calculating and storing $\hat{h}^{(i)}$ explicitly.

Very often one is not interested in the entire spectrum of $\hat{h}^{(i)}$ in the numerical basis.¹ For the calculation of the normal and pair densities, it is then sufficient to determine the Ω single-particle orbits with single-particle energies below the pairing cutoff, see Appendix A. For HF calculations, Ω does not have to be much larger than the number of nucleons. When pairing correlations are taken into account with an effective pairing interaction as defined in Refs. [37,38], the value for Ω in heavy nuclei is at most equal to twice the number of nucleons. This is

¹ A counterexample is the construction of the reference state for quasiparticle RPA and its various extensions.

several orders of magnitude smaller than the number of basis states N_m in the coordinate-space representation. In these conditions, iterative determination of the Ω lowest single-particle states is significantly less demanding in both CPU time and memory requirements than direct diagonalisation of $\hat{h}^{(i)}$ in a basis of dimension N_m .

Restricting the eigenvalue problem of Eq. (36) to the Ω lowest states allows us to recast the problem. Consider the Rayleigh quotient associated with the single-particle Hamiltonian

$$R_h(|\psi_\ell\rangle) = \frac{\langle\psi_\ell|\hat{h}^{(i)}|\psi_\ell\rangle}{\langle\psi_\ell|\psi_\ell\rangle}. \quad (38)$$

It can be shown [39] that the stationary points of R_h correspond to the eigenstates of \hat{h} , and that at these points, R_h is equal to the corresponding eigenvalue $\epsilon_\ell^{\text{ex}}$. Further we define

$$R_h^{\text{tot}}(|\psi_1\rangle, |\psi_2\rangle, \dots, |\psi_\Omega\rangle) = \sum_{\ell=1}^{\Omega} R_h(|\psi_\ell\rangle). \quad (39)$$

With the constraint on orthonormality of the single-particle orbitals, Eq. (37), any set of Ω eigenstates of $\hat{h}^{(i)}$ is a stationary point of R_h^{tot} . In particular, we have for a set of indices $\ell_1, \dots, \ell_\Omega$

$$R_h^{\text{tot}}(|\psi_{\ell_1}^{\text{ex}}\rangle, |\psi_{\ell_2}^{\text{ex}}\rangle, \dots, |\psi_{\ell_\Omega}^{\text{ex}}\rangle) = \sum_{m=1}^{\Omega} \epsilon_{\ell_m}^{\text{ex}} \quad (40)$$

where different ℓ label the many local minima of R_h^{tot} . Each corresponds to a different combination of Ω eigenstates of \hat{h} in the complete N_m -dimensional space. The absolute minimum of R_h^{tot} is obtained for the Ω single-particle states corresponding to the lowest eigenvalues of \hat{h} . For these we have

$$\min_{|\psi_{\ell_1}\rangle, |\psi_{\ell_2}\rangle, \dots, |\psi_{\ell_\Omega}\rangle} R_h^{\text{tot}} = \sum_{m=1}^{\Omega} \epsilon_m^{\text{ex}}. \quad (41)$$

The eigenvalue problem in Eq. (36) can be recast as a constrained optimization problem

$$\begin{aligned} \{|\psi_1^{\text{ex}}\rangle, |\psi_2^{\text{ex}}\rangle, \dots, |\psi_\Omega^{\text{ex}}\rangle\} &= \arg \min [R_h^{\text{tot}}], \\ &\text{subject to } \langle\psi_k^{\text{ex}}|\psi_\ell^{\text{ex}}\rangle = \delta_{k\ell}. \end{aligned} \quad (42)$$

From Eq. (42), it follows that the eigenvalue problem can be solved by iterative methods. We introduce a second iteration counter j that labels the evolution of the single-particle wave functions

$$|\psi_1^{(i,j)}\rangle, |\psi_2^{(i,j)}\rangle, \dots, |\psi_\Omega^{(i,j)}\rangle. \quad (43)$$

The natural starting point for the iterative diagonalisation is the set of single-particle orbitals from the previous SCF iteration, $|\psi_\ell^{(i,0)}\rangle = |\psi_\ell^{(i-1)}\rangle$.

In the context of self-consistent mean-field models for which the diagonalisation is embedded into an SCF iteration, an approximate diagonalisation of \hat{h} is in general

sufficient: instead of limiting the number of iterations by a convergence criterion the number of iterations is fixed to a maximum number j_{\max} .

The simplest iterative optimization technique is the method of gradient descent [40], which is frequently used for calculations involving EDFs [10, 15, 41], although sometimes with modifications as in [9, 42].

We first discuss this algorithm and analyse its performance for Skyrme functionals at NLO and N2LO. Then, we will show how to improve on its convergence with a minor change in the algorithm that leads to a scheme dubbed *heavy ball dynamics* in the literature.

3.2 Gradient descent and heavy-ball dynamics for quadratic forms

Focussing on the problem of diagonalisation, we first sketch both gradient descent and heavy-ball dynamics for a schematic problem that often serves as a laboratory for the analysis of minimisation algorithms [40, 43, 44].

Consider a quadratic form for a positive definite and symmetric matrix A and a vector \mathbf{b} on a (unspecified) vector space [43]

$$f(\mathbf{x}) = \frac{1}{2} \mathbf{x}^T A \mathbf{x} - \mathbf{b}^T \mathbf{x}. \quad (44)$$

The minimum of f is reached for

$$\mathbf{x}^{(\infty)} = A^{-1} \mathbf{b}. \quad (45)$$

The minima of f coincide with the zeros of its first derivative with respect to \mathbf{x}

$$\frac{\partial f}{\partial \mathbf{x}} = A \mathbf{x} - \mathbf{b}. \quad (46)$$

minimising the function f is thus equivalent to solving the system of coupled linear equations posed by setting Eq. (46) to zero.

An iterative solution of the minimisation is most easily analysed using a transformed variable \mathbf{y}

$$\mathbf{y} = \mathbf{x} - A^{-1} \mathbf{b}, \quad (47)$$

so that we have

$$f(\mathbf{y}) = \frac{1}{2} \mathbf{y}^T A \mathbf{y}, \quad \frac{\partial f}{\partial \mathbf{y}} = A \mathbf{y}. \quad (48)$$

At the solution of the minimisation problem, $\mathbf{x} = \mathbf{x}^{(\infty)}$, $\mathbf{y} = 0$. An efficient iterative scheme should thus provide an evolution of the transformed variable, such that $\mathbf{y} \rightarrow 0$ as quickly as possible. We will demonstrate below that the spectrum of eigenvalues of A , denoted by λ_n , strongly influences the possible convergence rate. In particular, the condition number of A will play a crucial role. It is defined as the ratio between the largest and the lowest eigenvalues

$$\kappa^A = \frac{\lambda_{\max}}{\lambda_1}. \quad (49)$$

Gradient descent. Starting from an initial guess $\mathbf{x}^{(0)}$, the gradient-descent update from iteration j to iteration $j+1$ is given by

$$\begin{aligned} \mathbf{x}^{(j+1)} &= \mathbf{x}^{(j)} - \alpha \left. \frac{\partial f}{\partial \mathbf{x}} \right|_{\mathbf{x}=\mathbf{x}^{(j)}} \\ &= \mathbf{x}^{(j)} - \alpha (A \mathbf{x}^{(j)} - \mathbf{b}), \end{aligned} \quad (50)$$

where α is a numerical parameter still to be specified. The evolution in terms of the variable \mathbf{y} can be developed into the eigenvectors \mathbf{x}_k^A of A

$$\mathbf{y}^{(j)} = \sum_k a_k^{(j)} \mathbf{x}_k^A. \quad (51)$$

Inserting this into Eq. (50), we obtain for the expansion coefficients $a_k^{(j)}$

$$a_k^{(j+1)} = (1 - \alpha \lambda_k) a_k^{(j)}. \quad (52)$$

One can obtain the expansion coefficients at iteration (j) from the initial value at iteration (0) by applying j times $(1 - \alpha \lambda_k)$

$$a_k^{(j)} = (1 - \alpha \lambda_k)^j a_k^{(0)}. \quad (53)$$

Under the condition that

$$0 < \alpha < \frac{2}{\lambda_{\max}}, \quad (54)$$

the value of $|1 - \alpha \lambda_k|$ is smaller than one, and the components of \mathbf{y} in Eq. (53) decay exponentially to zero at a rate that increases for larger eigenvalues. For this reason, the coefficient $a_1^{(j)}$ tends to zero the slowest out of all a_k .

The overall rate of convergence is thus determined by $-\alpha \lambda_1$. Combined with Eq. (54), this means that it is the spread in eigenvalues of A that governs the convergence of the gradient-descent method. When the condition number, Eq. (49) of A is large, gradient descent converges only slowly to the optimum of the function f .

Heavy-ball dynamics. In Ref. [45], B. T. Polyak proposed the heavy-ball algorithm to improve on the convergence behaviour of the gradient-descent method for the iterative solution of systems of linear equations. The heavy-ball update scheme is given by

$$\begin{aligned} \mathbf{x}^{(j+1)} &= \mathbf{x}^{(j)} - \alpha (A \mathbf{x}^{(j)} - \mathbf{b}) + \mu \delta \mathbf{x}^{(j)}, \\ \delta \mathbf{x}^{(j)} &= (\mathbf{x}^{(j)} - \mathbf{x}^{(j-1)}). \end{aligned} \quad (55)$$

Compared to gradient descent, there is an additional $\mu \delta \mathbf{x}^{(j)}$ term, which is usually called the *momentum term*, while μ is called the *momentum parameter*. This term introduces a memory effect that allows for speeding up the iterative process.

The analysis of this method is more involved than that of the gradient-descent method. As discussed in Refs. [43,

44], the algorithm converges to the minimum of f on the condition that

$$0 \leq \mu < 1, \quad 0 < \alpha < \frac{2}{\lambda_{\max}}(1 + \mu). \quad (56)$$

The components of the variable \mathbf{y} of Eq. (47) evolve according to

$$\begin{aligned} a_k^{(j+1)} &= a_k^{(j)} + v_k^{(j)}, \\ v_k^{(j)} &= -\alpha \lambda_k a_k^{(j)} + \mu(a_k^{(j)} - a_k^{(j-1)}). \end{aligned} \quad (57)$$

The evolution determined by Eq. (57) is analogous to the one of a damped harmonic oscillator, as outlined in Appendix B. Three different regimes can be distinguished depending on the value of μ : the motion of $a_k^{(j+1)}$ can either be *underdamped*, *overdamped* or *critically damped*. For a given value of α , the critical momentum value μ_k^{crit} separating the regimes is given by

$$\mu_k^{\text{crit}} = \left(1 - \sqrt{\alpha \lambda_k}\right)^2. \quad (58)$$

If $\mu > \mu_k^{\text{crit}}$, the motion of a_k is underdamped: a_k undergoes slowly decaying oscillations around zero as a function of the iterations. By contrast, if $\mu < \mu_k^{\text{crit}}$, the motion of a_k is overdamped. In this case, the coefficient a_k does not oscillate, but decays exponentially to zero as for gradient descent. When $\mu = \mu_k^{\text{crit}}$, the motion is critically damped. For this particular value of the momentum parameter μ , the coefficient a_k decays to zero significantly faster than in the other two cases.

However, the critical value for μ_k^{crit} is different for every a_k . It can be shown that the optimal compromise in terms of convergence rate of the errors between small eigenvalues and large eigenvalues is given by [44]

$$\mu_{\text{opt}}^A = \left(\frac{\sqrt{\kappa^A} - 1}{\sqrt{\kappa^A} + 1}\right)^2. \quad (59)$$

The optimal value of α to be used in conjunction with this value of the momentum parameter is [43]

$$\begin{aligned} \alpha_{\text{opt}}^A &= \left(\frac{2}{\sqrt{\lambda_{\max}} + \sqrt{\lambda_1}}\right)^2 \\ &= \frac{2}{\lambda_{\max}}(1 + \mu_{\text{opt}}^A) - \frac{1}{\kappa^A} \left(\frac{2}{\sqrt{\lambda_{\max}} + \sqrt{\lambda_1}}\right)^2, \end{aligned} \quad (60)$$

where the second equality can be shown with straightforward algebra. This optimal value for α is virtually equal to the upper limit dictated by Eq. (56), because in most cases of interest κ^A is large.

The optimal iterative parameters of the method are thus closely related to the condition number κ^A of A , Eq (49): when κ^A is high, the momentum parameter μ should be taken close to 1. In such case, the size of α can be nearly doubled compared to gradient descent, resulting in much faster convergence.

However, the advantage of heavy-ball dynamics over gradient descent goes beyond the factor two on the upper limit of α , as will be demonstrated with practical examples in Section 5. One can prove that heavy-ball dynamics [43,46] with optimal parameters $(\alpha_{\text{opt}}^A, \mu_{\text{opt}}^A)$, achieves the fastest convergence rate that is theoretically possible across a range of similar methods: it is impossible to do better using algorithms that only incorporate information on the first-order derivatives of the quadratic form given by Eq. (44).

3.3 The gradient descent method applied to the diagonalisation subproblem

The schematic problem discussed in Section 3.2 is a simplification of the self-consistent mean-field problem that we want to solve. Nevertheless, both gradient descent and heavy-ball dynamics can be employed with only minor modifications.

The gradient of the Rayleigh quotient, Eq. (38), R_h^{tot} with respect to the ℓ -th single-particle wave function is given by

$$\left. \frac{\partial R_h^{\text{tot}}}{\partial |\psi_\ell\rangle} \right|_{|\psi_\ell\rangle=|\psi_\ell^{(i,j)}\rangle} = (\hat{h}^{(i)} - \epsilon_\ell^{(i,j)}) |\psi_\ell^{(i,j)}\rangle, \quad (61)$$

taking into account that $|\psi_\ell^{(i,j)}\rangle$ is normalized and where $\epsilon_\ell^{(i,j)}$ is the ℓ -th diagonal matrix element of $\hat{h}^{(i)}$

$$\epsilon_\ell^{(i,j)} = \langle \psi_\ell^{(i,j)} | \hat{h}^{(i)} | \psi_\ell^{(i,j)} \rangle. \quad (62)$$

The gradient-descent update from iteration j to $j+1$ for the ℓ -th single-particle wave function is then given by

$$|\phi_\ell^{(i,j+1)}\rangle = |\psi_\ell^{(i,j)}\rangle - \frac{dt}{\hbar} (\hat{h}^{(i)} - \epsilon_\ell^{(i,j)}) |\psi_\ell^{(i,j)}\rangle. \quad (63)$$

The $|\phi_\ell^{(i,j+1)}\rangle$ do not constitute an orthonormal set, even if the $|\psi_\ell^{(i,j)}\rangle$ do. For this reason, the algorithm needs to be complemented by an explicit orthonormalisation step that transforms the set of $|\phi_\ell^{(i,j)}\rangle$ into an orthonormal set $|\psi_\ell^{(i,j)}\rangle$ by, for instance, a Gram-Schmidt process. This step can be seen as a projection on a feasible set [40]; a more precise name for the algorithm would in fact be *projected gradient descent*. An alternative to the orthonormalisation step is to add a set of Lagrange constraints to the optimization problem in Eq. (42), as for example done in Ref. [47].

In the context of nuclear mean-field methods, the gradient-descent evolution of the single-particle wave functions was originally derived from the first-order approximation to the operator of evolution in imaginary time [41]. For this historical reason we have replaced the step size α by dt/\hbar . The gradient descent method is often called *imaginary time evolution* [10]. In other fields of physics, such appellation is used for more advanced techniques to approximate the exponentiation of the single-particle Hamiltonian [48].

The similarities between the simpler problem of Section 3.2 and the mean-field problem are revealed by comparing Eqs. (61) and (50): the gradient of the Rayleigh quotient is similar to that of a quadratic form, where $\hat{h}^{(i)}$ plays the role of the matrix A . There are however two important differences: the first one is that the second term in Eq. (61) varies from one iteration to the next, whereas the vector \mathbf{b} was kept fixed in Eq. (50). The second difference is that the self-consistent problem requires the evolution of many single-particle wave functions, constrained to be orthonormal, whereas we considered only one vector \mathbf{x} in Section 3.2. Because of these differences, we cannot provide an analytical formula of the evolution of the single-particle wave functions, whereas for the simplified problem we are able to write down Eq. (53).

As for the schematic problem of Section 3.2, the gradient-descent method only converges for a limited range of values of dt . For fast convergence, it is advisable to use the largest feasible value. Since for all ℓ one has $\epsilon_\ell^{(i,j)} > \epsilon_1^{\text{ex}}$, the value of $\epsilon_{\text{max}}^{\text{ex}} - \epsilon_1^{\text{ex}}$ is an upper bound for the largest eigenvalue of $(\hat{h}^{(i)} - \epsilon_\ell^{(i,j)})$. By analogy to the schematic problem, we obtain a condition on dt

$$\frac{dt}{\hbar} < \frac{2}{\epsilon_{\text{max}}^{\text{ex}} - \epsilon_1^{\text{ex}}}, \quad (64)$$

see also the discussion in Refs. [2, 10, 41, 42]. Unfortunately, Eq. (64) does not offer a practical way of selecting dt at the first iteration. While $\epsilon_1^{(i,0)}$ is in general a sufficient estimate of ϵ_1^{ex} , no information is available on $\epsilon_{\text{max}}^{\text{ex}}$.

A robust way to judge the convergence of the diagonalisation subproblem is evaluating the weighted dispersion of the single-particle energies $(dh^2)^{(i,j)}$, defined as

$$(dh^2)^{(i,j)} = \frac{1}{A} \sum_{\ell=1}^{\Omega} \rho_{\ell\ell} \left[\langle \psi_\ell^{(i,j)} | (\hat{h}^{(i)})^\dagger \hat{h}^{(i)} | \psi_\ell^{(i,j)} \rangle - (\epsilon_j^{(i,j)})^2 \right]. \quad (65)$$

Weighting the individual contributions by the diagonal matrix element of the density matrix $\rho_{\ell\ell}$ [12] limits the sum to those single-particle states that contribute to observables. Small (large) values of this quantity indicate that the single-particle wave functions at iterations (i, j) are good (bad) approximations to the eigenstates of $\hat{h}^{(i)}$.

3.4 The choice of dt and the largest eigenvalue of $\hat{h}^{(i)}$

The upper end of the spectrum of $\hat{h}^{(i)}$ depends not only on the parametrisation employed and the numerical representation of the single-particle wave functions, but in a weaker way also on the particular configuration of potentials at iteration (i) . For a general case, a precise analysis is not straightforward. Some inferences can be made based on the operator structure of the single-particle Hamiltonian, which in turn is determined by the operator structure of the local densities through Eq. (25).

For NLO Skyrme EDFs, such analyses have been made before, see for instance [12, 42]. In that case, the maximal

eigenvalue of $\hat{h}^{(i)}$ is dominated by the kinetic energy of the corresponding eigenstate. The variation of the energy with respect to $\tau(\mathbf{r})$ results in the presence of a Laplacian operator in the single-particle Hamiltonian $\hat{h}^{(i)}$. Whereas other terms from Eq. (18) also contribute to the potential $F^\tau(\mathbf{r})$, and a Laplacian operator also appears in the time-odd term multiplied by $F^T(\mathbf{r})$, the contribution from the kinetic energy, Eq. (14), can be expected to be by far the dominant one, as otherwise one would work with a parametrisation whose effective mass takes an unrealistic value in one of the various spin-isospin channels.

The largest kinetic energy is found for the oscillatory mode with the shortest wavelength that can be represented in the chosen numerical representation. In a coordinate-space representation using an equidistant mesh as done here, the analysis is straightforward: the state that oscillates the most quickly has one node less than there are mesh points. On a mesh with spacing dx , the momentum of a state $|\psi^{\mathbf{k}_{\text{max}}}\rangle$ with wavelength $2dx$ therefore provides an upper bound for the maximum momentum \mathbf{k}_{max}

$$|\mathbf{k}_{\text{max}}|^2 \lesssim 3 \frac{\pi^2}{dx^2}, \quad (66)$$

where the factor 3 arises from the contributions of all Cartesian directions. In that case the maximal eigenvalue of $\hat{h}^{(i)}$ scales with the mesh spacing as

$$\epsilon_{\text{max}}^{\text{NLO}} \simeq -\frac{\hbar^2}{2m} \langle \psi^{\mathbf{k}_{\text{max}}} | \Delta | \psi^{\mathbf{k}_{\text{max}}} \rangle = \frac{\hbar^2}{2m} \frac{3\pi^2}{dx^2}. \quad (67)$$

Inserting relation (67) into Eq. (64), one finds that the maximal allowed value of dt decreases quadratically with the mesh spacing, as was discussed in [10, 12].

For N2LO functionals, the analysis is much less clear cut. Compared to the NLO case, there are additional contributions with two gradients to the single-particle Hamiltonian, Eq. (30), that have a more complicated tensor structure than the NLO terms. More importantly for our analysis, there are also terms with three or four gradients acting on the wave function in Eq. (30). The contribution of those containing three gradients to the highest eigenvalue of $\hat{h}^{(i)}$ scales as $|\mathbf{k}_{\text{max}}|^3$, and those with four gradients even scale with $|\mathbf{k}_{\text{max}}|^4$. Because of the contribution from the kinetic energy, $F^\tau(\mathbf{r})$ can be expected to be positive and the dominant one among terms with two gradients. By contrast, the potentials specific to N2LO can all have either sign. For given \mathbf{k}_{max} , the dominant contribution to the highest eigenvalue of $\hat{h}^{(i)}$ depends then on the relative sizes and signs of the various N2LO potentials when compared to $F^\tau(\mathbf{r})$.

In the most unfavourable scenario, $F^Q(\mathbf{r})$ is positive and of a size that makes $\langle \psi^{\mathbf{k}_{\text{max}}} | F^Q \Delta | \psi^{\mathbf{k}_{\text{max}}} \rangle$ a large positive number, such that the largest single-particle energy that can be represented on the mesh scales with dx^{-4} instead of dx^{-2} , leading to larger values $\epsilon_{\text{max}}^{\text{N2LO}}$ than what is estimated for NLO functionals, Eq. (67). The step size dt of the gradient descent for the diagonalisation subproblem then has to be reduced accordingly, slowing down the convergence rate.

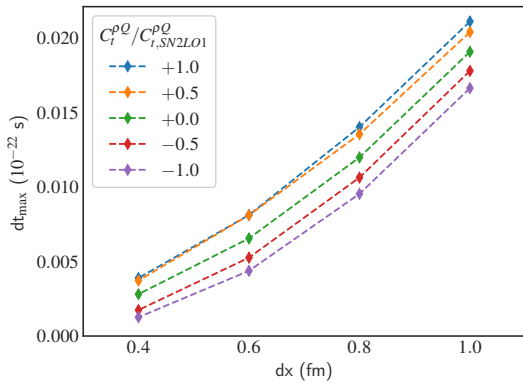


Fig. 2. Maximum value of dt for which gradient-descent calculations of ^{40}Ca converge for a modified SN2LO1 interaction (see text) as a function of dx , for different values of the N2LO coupling constants $C_0^{\rho Q}$ and $C_1^{\rho Q}$.

More importantly, because of the parametrisation-dependence of the relative sizes and signs of the potentials multiplying three and four gradients, for future N2LO parametrisations we have to expect a wide variation in the largest eigenvalues of $\hat{h}^{(i)}$ on a given mesh. This, in turn, will lead to a large spread in the performance of gradient descent for the diagonalisation subproblem. To illustrate this point, we have constructed a set of toy N2LO parametrisations based on the SN2LO1 parametrisation [8], for which all of the N2LO coupling constants have been set to zero, except for $C_0^{\rho Q}$ and $C_1^{\rho Q}$. Figure 2 shows the largest value of dt for which a gradient-descent calculation for ^{40}Ca converges, as a function of the mesh discretization dx . When $C_0^{\rho Q} = C_1^{\rho Q} = 0$, the toy parametrisation does not contain N2LO terms anymore, such that the curve represents the typical behaviour found at NLO. For non-zero values of the N2LO coupling constants, and depending on their sign, the maximal allowable value of dt either increases or decreases with respect to the NLO curve. This variation is quite large; at $dx = 0.8$ fm, there is a factor of about two difference in dt (and hence convergence rate) when changing the sign of $C_0^{\rho Q}$ and $C_1^{\rho Q}$. Even for this modest range of coupling constants, the sensitivity of the maximal value dt is rather high, a situation that is not desirable at all when dt has to be set by hand.

3.5 Heavy-ball dynamics for the diagonalisation subproblem

The heavy-ball update from iteration j to iteration $j + 1$ for the ℓ -th single-particle wave function is given by²

$$|\delta\psi_\ell^{(i,j)}\rangle = |\psi_\ell^{(i,j)}\rangle - |\psi_\ell^{(i,j-1)}\rangle \quad (\text{if } j \neq 0), \quad (68)$$

$$|v_\ell^{(i,j)}\rangle = -\frac{dt}{\hbar} \left(\hat{h}^{(i)} - \epsilon_\ell^{(i,j)} \right) |\psi_\ell^{(i,j)}\rangle + \mu |\delta\psi_\ell^{(i,j)}\rangle, \quad (69)$$

² We recall that the index i labels the iterations of the SCF subproblem where the single particle Hamiltonian $\hat{h}^{(i)}$ is updated and j labels the iterations of the diagonalisation of $\hat{h}^{(i)}$.

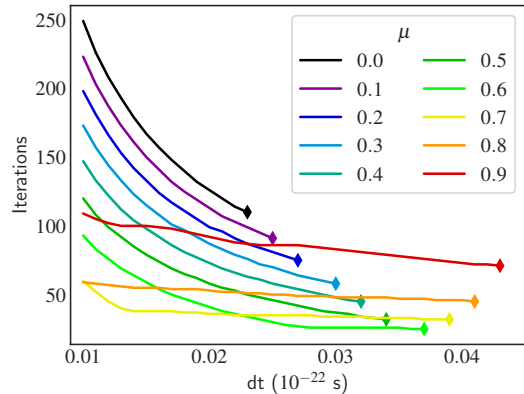


Fig. 3. Number of iterations needed to reach a weighted dispersion $(dh^2)^{(0,j)} = 10^{-5}$ MeV² as a function of dt and μ , without updating mean-field densities and potentials. The nucleus under consideration is ^{16}O in a box with $N_x = N_y = N_z = 24$ at $dx = 0.8$ fm using the SLy4 parametrisation of the Skyrme NLO EDF. All calculations were initialized using spherical Nilsson orbitals. The last point on every line, marked by a diamond, is the highest value of dt for which we were able to converge the calculation.

$$|\phi_\ell^{(i,j+1)}\rangle = |\psi_\ell^{(i,j)}\rangle + |v_\ell^{(i,j)}\rangle. \quad (70)$$

For the first iteration, $j = 0$, one initializes $|\delta\psi_\ell^{(i,0)}\rangle$ with $|\delta\psi_\ell^{(i-1,j_f)}\rangle$ from the last iteration j_f performed with the previous Hamiltonian $\hat{h}^{(i-1)}$. An orthonormalization of the single-particle wave functions $|\phi_\ell\rangle \rightarrow |\psi_\ell\rangle$ is also needed at each iteration. Compared to the gradient-descent method, this algorithm does not require extra CPU time, but only extra storage of the auxiliary variables $|\delta\psi_\ell^{(i,j)}\rangle$.

We expect from Eq. (56) that the algorithm converges under the condition that

$$0 \leq \mu < 1, \quad \frac{dt}{\hbar} < \frac{2(1+\mu)}{\epsilon_{\max}^{\text{ex}} - \epsilon_1^{\text{ex}}}. \quad (71)$$

Figure 3 illustrates the dependence of the convergence speed on the specific choices made for dt and μ for the case of the diagonalisation subproblem of ^{16}O . For a given μ , the amount of iterations needed to converge is smallest for values of dt just below the ceiling value of Eq. (71). As μ increases, the ceiling value for dt increases as well, until for $\mu = 0.9$ it almost doubles compared to the gradient descent case. The overall minimum of iterations needed is, however, achieved for a specific value of μ , here close to 0.6.

The heavy-ball method has the same drawback as the gradient-descent method: the optimal selection of dt depends on the numerical basis and the form and parametrisation of the EDF. To complicate the situation, the additional parameter μ also impacts the convergence rate. In the next section, we propose an algorithm to select appropriate values of the iterative parameters dynamically during the optimization process.

3.6 Dynamical update of the iteration parameters

We are not aware of a theoretical study to find the optimal parameters for either gradient descent or heavy-ball dynamics applied to an optimization problem similar to that of Eq. (42). We therefore propose, without detailed analysis, a few simple formulas that are inspired by the results of Section 3.2 and which can be used to dynamically estimate appropriate numerical parameters at every SCF iteration (i), eliminating all need for human fine-tuning.

For both algorithms, we first need an estimate for the largest eigenvalue of the single-particle Hamiltonian, $\epsilon_{\max}^{\text{ex}}$. For its determination, we introduce an extra single-particle wave function $|\psi_{\text{aux}}^{(i)}\rangle$ that does not participate in the evolution of the single-particle states the nuclear observables are calculated from. Introducing a third iteration counter (k), we evolve this auxiliary wave function with the so-called power-iteration scheme [39]

$$|\psi_{\text{aux}}^{(i,k+1)}\rangle = \frac{1}{\langle \psi_{\text{aux}}^{(i,k)} | \hat{h}^{(i)} | \psi_{\text{aux}}^{(i,k)} \rangle} \hat{h}^{(i)} |\psi_{\text{aux}}^{(i,k)}\rangle. \quad (72)$$

For $k \rightarrow \infty$, $|\psi_{\text{aux}}^{(i,k)}\rangle$ will converge to the eigenstate with largest possible eigenvalue $\tilde{\epsilon}_{\max}^{(i)}$ of $\hat{h}^{(i)}$. In practice, one does not have to reach large accuracy to obtain an estimate of

$$\tilde{\epsilon}_{\max}^{(i)} \equiv \langle \psi_{\text{aux}}^{(i,\infty)} | \hat{h}^{(i)} | \psi_{\text{aux}}^{(i,\infty)} \rangle \quad (73)$$

that serves our purpose. In general, a few iterations of Eq. (72) suffice to determine $\tilde{\epsilon}_{\max}^{(i)}$ to within a few MeV. The converged auxiliary state from the previous SCF iteration ($i-1$) can be used as starting point at iteration (i). As $|\psi_{\text{aux}}^{(i)}\rangle$ is a highly oscillatory state, at the very first SCF iteration it can be initialized using a random number generator.

For heavy-ball dynamics, we also need to estimate the momentum parameter. By analogy to Eq. (59), we propose to set

$$\mu_{\text{dyn}}^{(i)} = \left(\frac{\sqrt{\kappa^{(i)}} - 1}{\sqrt{\kappa^{(i)}} + 1} \right)^2, \quad (74)$$

where $\kappa^{(i)}$ is the analogue of the condition number of the matrix A in Section 3.2. Because of the simultaneous optimization of many eigenvalues under an orthogonality constraint, we cannot use Eq. (49). After some numerical experimentation, we have adopted the prescription

$$\kappa^{(i)} = \frac{\tilde{\epsilon}_{\max}^{(i)} - \epsilon_1^{(i)}}{E_{\min}^{\text{qp},(i)}}, \quad (75)$$

where $\tilde{\epsilon}_{\max}$ is given by Eq. (73) and $E_{\min}^{\text{qp},(i)}$ is the smallest positive quasiparticle energy of the HFB Hamiltonian. In our experience, Eq. (75) provides a robust estimate for $\mu_{\text{dyn}}^{(i)}$ when fed into Eq. (74). This formula has been tailored for the optimization of the diagonalisation problem embedded into SCF iteration under the assumption that only the occupied single-particle states need to be

well converged. Other applications will require a different recipe.

Using Eq. (74) to calculate the momentum parameter, we set

$$\frac{dt_{\text{dyn}}^{(i)}}{\hbar} = s \frac{2(1 + \mu_{\text{dyn}}^{(i)})}{\tilde{\epsilon}_{\max}^{(i)} - \epsilon_1^{(i)}}, \quad (76)$$

where we introduced a factor $0 < s < 1$ to guarantee that Eq. (71) holds. To obtain a dynamical estimate for the step size for use in a gradient-descent approach, it is sufficient to set $\mu_{\text{dyn}}^{(i)} = 0$ in Eq. (76). In practice, we have empirically fixed the factor s to 0.9 in Eq. (76). This empirical choice guaranteed convergence in all of the many calculations we performed since implementing this scheme.

3.7 Comparison to other approaches

Gradient-based schemes are used by the nuclear physics community for decades, with [15, 41] being among the first detailed references describing the application of such methods to the self-consistent HF and HFB problems.

More advanced iterative methods have been developed since. One example is the nonlinear conjugate-gradient method [16]. Like the scheme described in Ref. [15], it is often used to address the diagonalisation and SCF subproblems simultaneously. Like many other advanced optimisation schemes [40], this method relies on an adaptive step size, which needs to be chosen in some optimal way at every iteration. Its determination is usually accomplished by some variation of a line-search method, which requires multiple evaluations of the total energy, each time for a different set of single-particle states. Compared to the simple gradient scheme described above, in coordinate-space representation, the necessary multiple construction of derivatives of single-particle states and summation of densities increases the numerical cost per iteration by a large factor, as these are the most costly tasks. Heavy-ball dynamics does not have this drawback, as it does not require any evaluation of the total energy or of single-particle matrix elements in addition to those already needed for the unmodified gradient descent.

As a last remark, we note that the heavy-ball update scheme presented here is quite similar to that of Car-Parrinello dynamics [49], a widely-used method in atomic density functional theory [50]. In Car-Parrinello dynamics, the analogue of the momentum parameter μ is usually called the fictitious electron mass, and has the same impact on the convergence rate. To the best of our knowledge, the only application of this method to a nuclear problem is described in Ref. [13].

3.8 Summary and MOCCA implementation

As mentioned before, for calculations performed on a 3d mesh, the diagonalisation subproblem is much more CPU intensive than the evolution of the mean-field potentials and densities because it requires to determine the derivatives of the single-particle wave functions. In practice, the

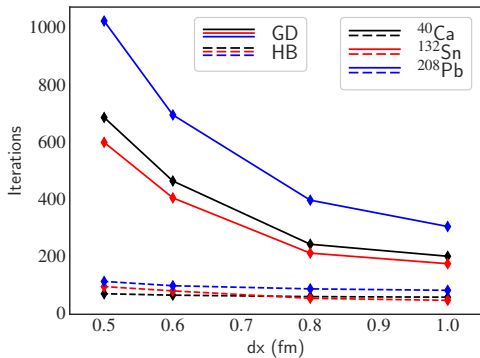


Fig. 4. Number of SCF iterations needed to achieve $(dh^2)^{(i,j)} \leq 10^{-5} \text{ MeV}^2$ for ^{40}Ca , ^{132}Sn and ^{208}Pb using the SLy5s1 parametrisation of the Skyrme NLO EDF as a function of the mesh discretization dx .

most appropriate choice is to restrict the diagonalisation of $\hat{h}^{(i)}$ to a single iteration, $j_{\max} = 1$. For this particular choice, the extra iteration index j is superfluous and we will drop it in what follows. The auxiliary variables in Eq. (70) become

$$|\delta\psi_\ell^{(i)}\rangle = |\psi_\ell^{(i)}\rangle - |\psi_\ell^{(i-1)}\rangle. \quad (77)$$

A single iteration (i) of the heavy-ball algorithm can be summarised as

1. Calculate $\tilde{\epsilon}_{\max}^{(i)}$, Eq. (73), by evolving $|\psi_{\text{aux}}^{(i,k)}\rangle$ according to Eq. (72), starting from $|\psi_{\text{aux}}^{(i-1)}\rangle$.
2. Calculate $dt_{\text{dyn}}^{(i)}$ and $\mu_{\text{dyn}}^{(i)}$ using Eqs. (76), (74).
3. Obtain all $|\phi_\ell^{i+1}\rangle$ from Eq. (70).
4. Orthonormalize to obtain the set of $|\psi_\ell^{(i+1)}\rangle$.
5. Calculate $|\delta\psi_\ell^{(i+1)}\rangle$ for use in the next iteration.

The gradient-descent algorithm consists of the same steps with $\mu_{\text{dyn}}^{(i)} = 0$.

The efficiency of the heavy-ball approach and the dynamical estimates for the numerical parameters proposed in Section 3.6, is illustrated by Fig. 4. It shows the number of iterations needed to converge the diagonalisation subproblem for three different spherical nuclei as a function of the mesh discretization dx . Results obtained with the gradient-descent algorithm and heavy-ball dynamics with dynamically estimated values for dt and μ are compared. Recalling that the computational time per iteration is virtually the same in both schemes, the heavy-ball algorithm is several times faster than the gradient-descent approach, and this for all mesh discretizations dx . More strikingly, the number of iterations needed to converge the heavy-ball algorithm is (almost) independent of the mesh discretization. As discussed in Section 3.4, for the EDF used here the largest eigenvalue of the single-particle Hamiltonian increases with the inverse of the square of the mesh spacing, Eq. (66), increasing the spread in eigenvalues of the single-particle Hamiltonian. The maximal value of dt decreases for smaller dx , which significantly slows

down the gradient-descent algorithm. Heavy-ball dynamics with dynamically adjusted parameters is able to compensate for this spread, validating also the recipe provided by Eqs. (74) and (76).

4 The SCF Iterations

4.1 Position of the problem

We now investigate the second aspect of the solution of the self-consistent mean-field equations, which is the SCF subproblem of evolving the single-particle Hamiltonian from one self-consistent iteration to the next. For the sake of simple notation, we drop again the isospin index of densities and potentials.

As discussed in Section 2, the aim is to find the fixed point of the maps G^{R} and G^{F} . The most straightforward way to iterate the fixed-point problem of Eq. (33) is to calculate the mean-field densities and potentials of iteration ($i+1$) from the single-particle wave functions, obtained by the approximate diagonalisation of $\hat{h}^{(i)}$ in the previous iteration

$$\mathbf{F}^{(i+1)} = G^{\text{F}}(\mathbf{F}^{(i)}) = \mathbf{F}_{|\psi}^{(i+1)}, \quad (78)$$

$$\mathbf{R}^{(i+1)} = G^{\text{R}}(\mathbf{R}^{(i)}) = \mathbf{R}_{|\psi}^{(i+1)}, \quad (79)$$

where we use the notation $\mathbf{F}_{|\psi}^{(i+1)}$, $\mathbf{R}_{|\psi}^{(i+1)}$ to emphasize that the right-hand-sides of these relations are the potentials and fields obtained by direct calculation from the single-particle wave functions at iteration ($i+1$), using the formulas from Section 2.3. The scheme defined through Eqs. (78) and (79) does not lead to a stable iterative process, except in isolated cases. To understand why, consider the behaviour of the map given by Eq. (33) in the vicinity of a fixed point $\mathbf{F}^{(\infty)}$. If the error on the mean-field potentials is $\delta\mathbf{F}^{(i)}$, one can write

$$G^{\text{F}}(\mathbf{F}^{(\infty)} + \delta\mathbf{F}^{(i)}) \approx \mathbf{F}^{(\infty)} + \left. \frac{\partial G^{\text{F}}}{\partial \mathbf{F}} \right|_{\mathbf{F}=\mathbf{F}^{(\infty)}} \delta\mathbf{F}^{(i)}. \quad (80)$$

When Eq. (78) is used to generate a new set of potentials $\mathbf{F}^{(i+1)}$, the deviation from the fixed point at the next iteration can be approximated by

$$\delta\mathbf{F}^{(i+1)} = \mathbf{F}^{(i+1)} - \mathbf{F}^{(\infty)} \approx \mathbf{J}^{\text{F}} \delta\mathbf{F}^{(i)}, \quad (81)$$

where \mathbf{J}^{F} is the Jacobian of the problem for the potential \mathbf{F} at the fixed point,

$$\mathbf{J}_{ab}^{\text{F}} = \left. \frac{\partial G_a^{\text{F}}}{\partial \mathbf{F}_b} \right|_{\mathbf{F}=\mathbf{F}^{(\infty)}}. \quad (82)$$

In a similar fashion, we obtain for the mean-field densities $\mathbf{R}^{(i)}$ in the vicinity of the fixed point $\mathbf{R}^{(\infty)}$

$$\delta\mathbf{R}^{(i+1)} \approx \mathbf{J}^{\text{R}} \delta\mathbf{R}^{(i)}, \quad \mathbf{J}_{ab}^{\text{R}} = \left. \frac{\partial G_a^{\text{R}}}{\partial \mathbf{R}_b} \right|_{\mathbf{R}=\mathbf{R}^{(\infty)}}. \quad (83)$$

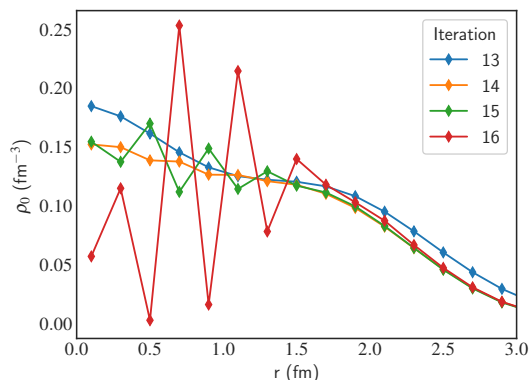


Fig. 5. Radial density profile of ^{40}Ca at iterations 13, 14, 15, and 16 for the SLy4 parametrisation of the Skyrme NLO EDF, with an SCF evolution directed by Eqs. (78) and (79). The diagonalisation subproblem was iterated with heavy-ball dynamics. At iteration 16, the energy is positive and the iterative process was stopped. The calculation was initialized using spherical Nilsson orbitals in a $(N_x, N_y, N_z) = (60, 60, 60)$ box with a mesh spacing of $dx = 0.2$ fm. We have chosen this mesh spacing for illustrative purposes only; it is significantly smaller than values that are typically used in practice ($dx \sim 0.8$ fm). The calculated values of the density on the mesh points are connected by straight lines to guide the eye.

Supposing that the linear approximation holds for all subsequent iterations, we obtain after N further iterations

$$\delta F^{(i+N)} \approx (J^F)^N \delta F^{(i)}, \quad (84)$$

$$\delta R_{q,a}^{(i+N)} \approx (J^R)^N \delta R^{(i)}. \quad (85)$$

This evolution only converges to a fixed point when the matrices J_q^F and J_q^R are contractive, that is if all of their eigenvalues are smaller than one in absolute size. When any eigenvalue is larger than one, then the iterative process in general diverges, as errors get amplified from one iteration to the next.

The problem of such divergences has been extensively discussed in the context of self-consistent calculations of atomic systems. In that case, the electron density can engage in long-wavelength oscillations from one iteration to the next, which is often called *charge sloshing*. Especially in metallic systems, where small changes in input electron density produce large changes in the output electron density, special measures need to be taken to safeguard convergence [51]. It is the spectrum of the Jacobians J^F and J^R , and through them the form of the interaction, that determines convergence: in the atomic case, the divergent modes are because of the long-range character of the Coulomb potential. For nuclear Skyrme EDFs, we show in the next section that the presence of external derivatives of local densities in the EDF, Eq. (15), gives rise to divergent short-wavelength modes.

The instability of the iterative scheme of Eqs. (78) and (79) because of short-wavelength changes in the density is illustrated by Fig. 5 for the NLO parametrization SLy4. The total density of ^{40}Ca obtained by SCF iterations directly using $F_{|\psi}^{(i+1)}$ and $R_{|\psi}^{(i+1)}$ is shown for iterations 13

to 16. At iteration 13 the central density still looks smooth. During the subsequent iterations, short wavelength deviations from the fixed point are quickly amplified by the iterative process: at iteration 14 small unphysical oscillations are visible and from iteration 16 onwards the corresponding total energy becomes positive.

Although the evolution of the densities with iteration number (i) is very similar, this instability is different in nature from the finite-size instabilities that have been studied for the Skyrme EDF in Refs. [52, 53, 54]. The divergence illustrated by Fig. 5 is entirely numerical, and its appearance a consequence of the iterative scheme unintentionally introducing oscillatory behaviour in the density that drives the system to a less bound state. By contrast, finite-size instabilities occur when the properties of an EDF parametrization are such that infinite inhomogeneous nuclear matter is more bound than the homogeneous phase and are thus a characteristic of a parametrization. All nuclear EDFs have to have such an instability in the $T = 0$, $S = 0$ channel, which is responsible for the formation of finite nuclei. However, it has recently been pointed out that many parametrizations of the nuclear EDF also exhibit non-physical finite-size instabilities in other S , T channels [52, 53, 54, 55, 56]. When these degrees of freedom can be resolved by the numerical representation used, the calculations are driven towards a highly oscillatory state that is more bound than a state with conventional density distribution, irrespective of the technique used to solve the mean-field equations. The numerical instability illustrated by Fig. 5, on the other hand, can be completely eliminated by adapting the iterative scheme, as we will show in what follows.

4.2 Highest eigenvalues of the Jacobians

Using the chain rule for derivatives, one can write for J^R

$$J_{ab}^R = \sum_c \left. \frac{\partial G(R)_a}{\partial F_c} \right|_{F=F(\infty)} \left. \frac{\partial F_c}{\partial R_b} \right|_{R=R(\infty)}. \quad (86)$$

and similarly for J^F . To obtain an idea of the behaviour of the second partial derivative in Eq. (86), consider a variation of the density $\rho(\mathbf{r})$ of the form

$$\delta\rho(\mathbf{r}) = a e^{i\mathbf{k}\cdot\mathbf{r}}, \quad (87)$$

where a is a small constant. For large values of $|\mathbf{k}|$, the variation in the potential $F^\rho(\mathbf{r})$ can be estimated to be

$$\begin{aligned} \delta F^\rho(\mathbf{r}) \approx & [2C^{\rho\rho} + (2 + \alpha)(1 + \alpha)C^{\rho\rho\rho^\alpha} \rho^\alpha(\mathbf{r}) \\ & - 2C^{\rho\Delta\rho} |\mathbf{k}|^2 + 2C^{\Delta\rho\Delta\rho} |\mathbf{k}|^4] \delta\rho(\mathbf{r}). \end{aligned} \quad (88)$$

where for sake of simple argument we omit the isospin structure of the single-particle Hamiltonian that couples perturbations in the density of one nucleon species to changes in the potentials of both species. Even if a is very small, such density components can make the evolution of the potentials divergent. The potentials F^ρ and F^s are the most volatile, since at a given order of functional (NLO,

N2LO or N3LO), they contain the highest number of external derivatives of a local density, which is either $\rho(\mathbf{r})$ or $\mathbf{s}(\mathbf{r})$.

In electronic structure calculations, the partial derivative of the output densities $G^R(\mathbf{R})$ with respect to the potentials F , that constitutes the other part of Eq. (86), is called the susceptibility [51]. It encodes the response of the system to a change of the potentials. In the context of EDF approaches, it is not obvious how to approximate this response efficiently: it depends sensitively on the changes in the single-particle wave functions that contribute to the densities. The eigenvalues of the matrices J^R depend in this way on the technique used to solve the diagonalisation subproblem. In our case, thanks to the iterative diagonalisation by either gradient-descent or heavy-ball dynamics, the change in the wave functions from one iteration to the next can be expected to be limited in size.

As discussed in Section 3 for the diagonalisation subproblem, it is the numerical representation that determines the scaling of the eigenvalues of J^R and J^F . In coordinate space, the largest representable \mathbf{k} can be estimated by Eq. (66). For an NLO functional, the largest eigenvalue of the Jacobian scales with dx^{-2} . For a general N2LO functional, the analysis depends on the balance between the contributions in Eq. (88). The first, and so far only, available N2LO parametrisation fitted to the properties finite nuclei, SN2LO1 [8], has coupling constants $C_t^{\Delta\rho\Delta\rho}$ that are both below 1.0 MeV. With this, they are much smaller than the almost one hundred MeV for this parametrisation's value of $C_0^{\rho\Delta\rho}$. As we show in the next section, for SN2LO1, the NLO terms dominate the eigenvalues of the SCF Jacobians for typical choices of dx .

4.3 Linear mixing

A simple method to achieve convergence, even in the presence of a Jacobian with large eigenvalues, is to perform a linear mixing between the updated potentials and densities and those from the previous iteration. We replace Eq. (78) and Eq. (79) with

$$F_a^{(i+1)} = F_a^{(i)} + \alpha^F \left[F_{a,|\psi}^{(i+1)} - F_a^{(i)} \right], \quad (89)$$

$$R_a^{(i+1)} = R_a^{(i)} + \alpha^R \left[R_{a,|\psi}^{(i+1)} - R_a^{(i)} \right], \quad (90)$$

where α^F and α^R are parameters between zero and one, which can be chosen differently for each density and potential. Using these equations to generate the evolution of the potentials and densities, the expression equivalent to Eqs. (84) and (85) become after N iterations

$$\delta F^{(i+N)} \approx [1 + \alpha_F (-1 + J^F)]^N \delta F^{(i)}, \quad (91)$$

$$\delta R^{(i+N)} \approx [1 + \alpha_R (-1 + J^R)]^N \delta R^{(i)}. \quad (92)$$

The appropriate size of these mixing constants is related to the maximum eigenvalues of the Jacobians, as discussed in the previous section.

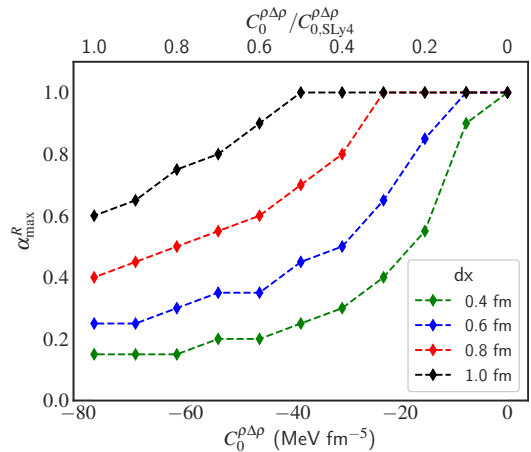


Fig. 6. Maximum value of α^R that results in a converged solution for a HF calculation of ^{40}Ca as a function of the coupling constant $C_0^{\rho\Delta\rho}$ for the first set of modified SLy4 parametrisations (see text). The convergence was tested by increasing α^R in steps of 0.05, such that values shown are lower limits and discontinuous.

To illustrate this, we have constructed two sets of modified versions of the SLy4 NLO parametrisation with systematically varied coupling constants of the time-even gradient terms. For the first set, the isovector terms are set to zero, $C_1^{\rho\Delta\rho} = 0$, while the original coupling constant of the isoscalar term $C_0^{\rho\Delta\rho}$ is multiplied with a scaling factor between zero and one. The second set fixes $C_0^{\rho\Delta\rho}$ at the value of the original parametrisation and scales the isovector coupling constant $C_1^{\rho\Delta\rho}$ instead. For reference, the original SLy4 values of the coupling constants are $C_0^{\rho\Delta\rho} = -76.996 \text{ MeV fm}^{-5}$ and $C_1^{\rho\Delta\rho} = 15.657 \text{ MeV fm}^{-5}$, respectively.

Using the first set of modified parametrisations, Fig. 6 shows the maximum value of α^R for which a calculation for ^{40}Ca converges for different mesh spacings dx , keeping $\alpha^F = 1$. For a Skyrme functional with $C_0^{\rho\Delta\rho} = C_1^{\rho\Delta\rho} = 0$, no mixing is necessary to converge the calculation for any choice of mesh spacing dx in our numerical representation, such that the SCF update parameter can be set to $\alpha^R = 1$. For finite $C_0^{\rho\Delta\rho}$, the value of α^R has to be reduced in order to obtain a stable iterative process. For given dx , the largest feasible α^R decreases when increasing the absolute value of $C_0^{\rho\Delta\rho}$, and it also decreases when diminishing dx for constant non-zero $C_0^{\rho\Delta\rho}$. For a typical choice of $dx = 0.8 \text{ fm}$, α^R has to be smaller than 0.4. For other configurations or other nuclei the ceiling value might be slightly different, such that a safe value that works for all cases has to be chosen even smaller.

Figure 7 shows the largest feasible value of α^R for the second set of parametrisations when varying $C_1^{\rho\Delta\rho}$ and dx . While the values of $C_0^{\rho\Delta\rho}$ are very similar for most parametrisations of the Skyrme NLO functional, those for $C_1^{\rho\Delta\rho}$ vary on a much wider scale. The ratio $C_1^{\rho\Delta\rho}/C_{1,\text{SLy4}}^{\rho\Delta\rho}$ cannot be increased by a large factor, though; when reach-

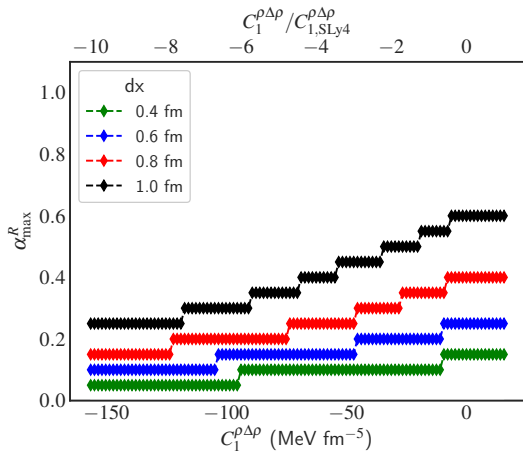


Fig. 7. Maximum value of α^R that results in a converged solution for a HF calculation of ^{40}Ca as a function of the coupling constant $C_1^{\rho\Delta\rho}$ for the second set of modified SLy4 parametrisations (see text). The convergence was tested by increasing α^R in steps of 0.05, such that values shown are lower limits and discontinuous. Note that $C_1^{\rho\Delta\rho}/C_{1,\text{SLy4}}^{\rho\Delta\rho} = 0$ corresponds to $C_0^{\rho\Delta\rho}/C_{0,\text{SLy4}}^{\rho\Delta\rho} = 1$ in Fig. 6.

ing values of about 2 the non-physical finite-size instabilities discussed in Refs. [52, 53, 54] set in. There are, however, some parametrisations for which $C_1^{\rho\Delta\rho}$ has the opposite sign and several times the absolute size compared to SLy4. Examples are UNEDF0 ($C_1^{\rho\Delta\rho} = -55.62 \text{ MeV fm}^{-5}$) [57], UNEDF1 ($C_1^{\rho\Delta\rho} = -145.38 \text{ MeV fm}^{-5}$) [58], and also UNEDF2 ($C_1^{\rho\Delta\rho} = -113.16 \text{ MeV fm}^{-5}$) [5]. The range of $C_1^{\rho\Delta\rho}$ covered in Fig. 7 extends to these values. When $C_1^{\rho\Delta\rho}$ becomes comparable to $C_0^{\rho\Delta\rho}$ in size and sign, the maximal feasible value of α^R has to be reduced below the value dictated by the isoscalar term alone.

Figures 6 and 7 address the possible interplay between the size of the coupling constants of the gradient terms and the possible choices for numerical parameters that control the convergence rate of SCF subproblem for the case of a time-reversal conserving calculation. When breaking time-reversal invariance, the analysis has also to consider the sign and size of the coupling constants $C_t^{s\Delta s}$, $t = 0, 1$, of the gradient terms of the spin density in Eq. (20). The corresponding terms behave very similar to the isovector term multiplied by $C_1^{\rho\Delta\rho}$: too large positive values of the $C_t^{s\Delta s}$ lead to non-physical finite-size instabilities, whereas for very large negative values of $C_t^{s\Delta s}$ the size of the mixing parameter α^R has to be adapted. In fact, the non-convergence of calculations for large, negative values of $C_t^{s\Delta s}$ reported in Ref. [26] can be remedied by lowering α^R below the value used in that study. When also including terms from a genuine contact tensor force in the Skyrme EDF [24, 26], there are additional second-order gradient terms containing the divergence of the the spin density that are to be considered in the analysis. For the N2LO Skyrme functional, Eq. (22), with its gradient terms that also contribute to other potentials the situation will

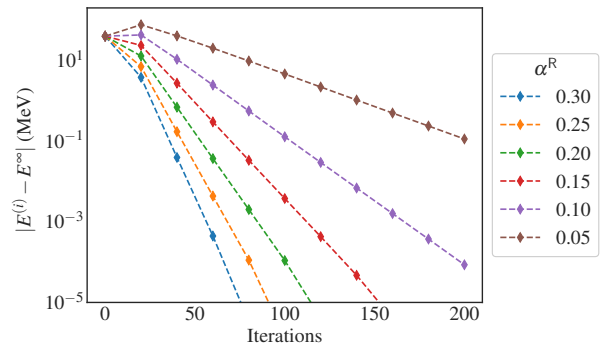


Fig. 8. (Color online) Difference between the energy at a given iteration $E^{(i)}$ and the energy after convergence $E^{(\infty)}$ for different values of α^R for a HF calculation of ^{40}Ca at $dx = 0.8 \text{ fm}$ with the SLy4 NLO parametrisation.

be further complicated, as is the case when considering three-body terms with gradients [28].

The parametrisation dependence of the largest possible mixing parameter α^R introduces a parametrisation dependence of the highest achievable convergence rate of the SCF iteration when using linear mixing of densities, Eq. (90), as smaller values of α^R inevitably slow it down. The difference can be quite substantial. This is illustrated by Fig. 8 that displays the error on the total binding energy of ^{40}Ca in a calculation with the original SLy4 parametrisation for different values of the mixing parameter α^R as a function of iteration number. For this choice of mesh with $dx = 0.8 \text{ fm}$, $\alpha^R = 0.3$ converges the calculation to the 0.01 keV level in about 70 iterations. In a calculation with $\alpha^R = 0.05$, after the same number of iterations the energy still changes on the 1 MeV level, and almost 1000 iterations will be needed to reach the level of 0.01 keV error.

The main advantage of linear mixing is its simplicity. It has, however, the serious limitation that the mixing parameter has to be fine-tuned to the parametrisation and mesh, resulting in vastly different convergence rates in different circumstances. To the best of our knowledge, no heuristic exists for selecting parameters prior to a calculation and manual experimentation is required to guarantee stability for a given combination of nucleus, mesh and EDF parametrisation while not needlessly sacrificing CPU time.

4.4 Preconditioning

All modes of the change of density are treated on an equal footing by linear mixing, irrespective of the size of their $|\mathbf{k}|$. In order to obtain an algorithm that allows for propagating long and short wavelength changes of the densities or potentials differently, we replace Eqs. (89) and (90) by

$$\mathbf{F}_a^{(i+1)} = \mathbf{F}_a^{(i)} + P^F \left[\mathbf{F}_{a,|\psi}^{(i+1)} - \mathbf{F}_a^{(i)} \right], \quad (93)$$

$$\mathbf{R}_a^{(i+1)} = \mathbf{R}_a^{(i)} + P^R \left[\mathbf{R}_{a,|\psi}^{(i+1)} - \mathbf{R}_a^{(i)} \right]. \quad (94)$$

The matrices P^F and P^R act as preconditioners of the fixed-point iteration. Their most useful form in general depends on the nature of the nuclear EDF, the chosen geometry and the numerical representation, and in general has to be a compromise between numerical efficiency, robustness, and numerical cost. We propose to use a preconditioner of the form

$$P^{F/R} = \left(1 - \beta^{F/R} \Delta\right)^{-1}, \quad (95)$$

where β^F and β^R are numerical parameters and Δ is the Laplacian. Both β^F and β^R must be positive, in order for the matrices P^R and P^F to be positive definite on the mesh.

To illustrate the effect of a preconditioner of the potential, P^F , take again as an example the response of the potential F^ρ of the Skyrme N2LO functional, Eq. (88), to a change of density of the form (87)

$$\delta F^{\rho,(i)} \approx [2 C^{\rho\rho} + (2 + \alpha)(1 + \alpha) C^{\rho\rho\rho^\alpha} \rho^\alpha(\mathbf{r}) - 2 C^{\rho\Delta\rho} |\mathbf{k}|^2 + 2 C^{\Delta\rho\Delta\rho} |\mathbf{k}|^4] [1 + \beta^F |\mathbf{k}|^2]^{-1} \delta\rho(\mathbf{r}) \quad (96)$$

For modes with small $|\mathbf{k}|$, P^F does not impede progress, as for those modes $P^F \approx 1$. When $|\mathbf{k}|$ is large, the preconditioning matrix slows down the oscillatory components, since $P^F \sim |\mathbf{k}|^{-2}$ in that case.

While in principle the preconditioning of the densities in Eq. (94) is a possible alternative to the preconditioning of the potentials, it is not as practical and well-behaved: there are stringent constraints on the mean-field densities that are not present for the potentials. The density $\rho(\mathbf{r})$, for example, needs to be positive everywhere while its integral has to be equal to the number of particles. Unlike the linear mixing of densities, Eq. (94) does not conserve such properties from one iteration to the next, requiring additional measures to rectify this issue. For this reason we set $\beta^R = 0$, placing the burden of slowing down the oscillatory modes completely on the preconditioning of the potentials.

We note in passing that the simple form of Eq. (93) is but one possible way to differentiate between changes in potentials of different wavelengths. For N2LO parametrizations with large values of $C_t^{\Delta\rho\Delta\rho}$ for instance, it might be of interest to incorporate an extra Laplacian in the preconditioning matrix. In fact, one can easily tailor more advanced prescriptions for different types of parametrizations or even employ different preconditioners for each individual contribution to the various potentials. Using Eq. (93) with an appropriate choice of β^F , however has sufficed to stabilize the SCF subproblem in all cases we have encountered so far.

4.5 Practical implementation and choice of β_F

Let us first discuss how to implement the preconditioning scheme. The matrix P^F is a full $(N_x \times N_y \times N_z) \times (N_x \times N_y \times N_z)$ matrix on the coordinate mesh, and storing it as well as performing the matrix multiplication in Eq. (93)

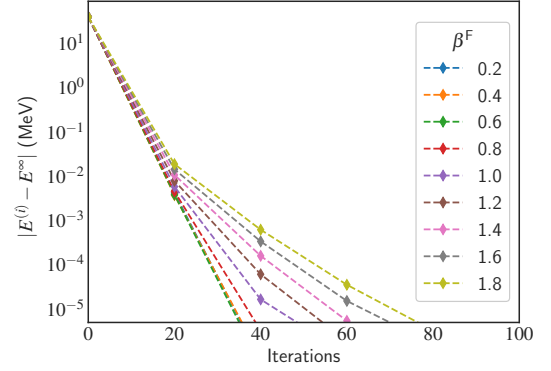


Fig. 9. Same as Fig. 8, but from a calculation using the potential preconditioner instead of linear mixing, for different values of the numerical parameter β^F entering Eq. (97).

would be prohibitively expensive. Its inverse, $(P^F)^{-1} = (1 - \beta^F \Delta)$, however, has a simple structure on the mesh, since the Laplacian is the sum of three separable matrices, see Eq. (10).

We obtain the update $F_a^{\text{update}} \equiv F_a^{(i+1)} - F_a^{(i)}$ of every preconditioned potential in Eq. (93) by solving the following linear system

$$(1 - \beta^F \Delta) F_a^{\text{update}} = [F_{a,|\psi}^{(i+1)} - F_a^{(i)}], \quad (97)$$

with a conjugate gradient method [40]. We obtain in this way the potentials at the next iteration, $F_a^{(i+1)} = F_a^{(i)} + F_a^{\text{update}}$, at the cost of only a few matrix multiplications with $(1 - \beta^F \Delta)$ for every mean-field potential.

In practice it is not even necessary to damp all of the mean-field potentials with a preconditioned update. It has sufficed in all calculations we performed so far to precondition only F_q^ρ and also F_q^s when time-reversal is broken. In this way, we only solve Eq. (97) for at most four real functions on the mesh and the numerical cost of the preconditioning is further reduced. In the end, the amount of applications of the Laplacian required to perform the preconditioning is negligible compared to the applications of the Laplacian to the full set of single-particle wave functions at every iteration.

Finally, let us discuss the choice of β^F . As with linear mixing, too small values render the iterative process unstable, whereas too large values unnecessarily slow down convergence. We have not succeeded in finding a way to optimize systematically the parameter β^F . The convergence speed of the fixed-point iteration is however significantly less sensitive to a fine-tuning of this parameter than in the case of linear mixing. Figure 9 shows the difference in the error on energy as a function of the iterations for SLy4 for different values of β^F . For $\beta^F < 0.1$, the iterative process is unstable. For larger values of β^F the convergence rate becomes progressively slower, but at a moderate pace: the overall convergence is not very sensitive to the precise value of β^F .

The value $\beta_F = 1.0$ has turned out to be an acceptably fast and stable for virtually all nuclei, parametrizations,

and choices of mesh discretization considered in this paper and all other calculations we performed with this scheme so far. The only exception we encountered so far is the UN-EDF1 parametrisation [58], which requires a larger value of $\beta^F \approx 1.8$ to reliably converge. This unusual behaviour is again a consequence of this parametrisation's large negative value of the coupling constant $C_1^{\rho\Delta\rho}$ (see Section 4.3), such that it sets the scale for numerical behaviour instead of $C_0^{\rho\Delta\rho}$, which is dominant for most other parametrisations.

4.6 Comments on some alternative approaches

Self-consistent density functional calculations in atomic physics have to safeguard the iterative process against long-wavelength oscillations of the electron density. The preconditioner proposed by Kerker [59] is widely used to suppress charge sloshing. It can be interpreted as a high-pass filter, whereas Eq. (93) represents a low-pass filter.

A preconditioner could in principle also be used for the diagonalisation subproblem. The iterative technique of *damped gradient iteration* proposed in Ref. [42, 60] can be viewed in this way: it combines gradient-descent and a pre-conditioning step, similar to Eq. (95), for the update of the single-particle wave functions. This technique is for example used in the Sky3D code [9]. The iterative scheme described in Ref. [17] utilises a preconditioning of quasiparticle wave functions in a gradient-based scheme to solve the HFB equations in that basis. In a representation like ours, the cost per iteration of preconditioning the states is much larger than that of preconditioning the potentials as it requires a much larger number of applications of derivative operators.

The two approaches (linear mixing and preconditioning) presented here use only information on the mean-field potentials and densities at iteration (i) to construct the potentials and densities at iteration ($i + 1$). Several techniques exist that aim to speed-up the convergence of the SCF subproblem by accounting for the mean-field potentials and densities from a larger number of past iterations. The Broyden method mixes potentials with a memory across multiple SCF iterations and has been successfully used to speed-up the convergence of EDF calculations in the existing solvers HFBTHO and HFODD [61]. Another method, mixing the densities across multiple SCF iterations is known either as *Pulay mixing* or the *direct inversion in the iterative subspace (DIIS)* method [32]. This method and several variants of it [62, 63] are widely used to accelerate self-consistent electronic structure calculations. Both methods, Broyden and DIIS, serve the purpose of accelerating the SCF convergence and do not by themselves guarantee a stable iterative process. These methods can be viewed as providing more advanced updates for the right hand sides of Eqs. (89) and (90), but both still incorporate a mixing parameter, similar to α^F and α^R , that has to be taken small enough to stabilise the iterative process. Although these methods have their qualities, we have limited ourselves to a detailed analysis of the approach that we have presented here, as it fulfils all our requirements: it

markedly improves the convergence speed without significant increase of the computational time per iteration or of the memory requirements, while being rather insensitive to the choice of numerical parameters.

5 Numerical tests

5.1 Conditions of the tests

The goal of this section is to compare the convergence properties of the schemes that we have developed in the two previous sections with what we have used in the past for typical situations encountered when calculating complex nuclei. The most detailed tests are performed with the SLy5s1 parametrisation of the Skyrme NLO functional [19], which provides a good description of the deformation properties of heavy nuclei [64]. For this parametrisation, we will study the convergence for calculations of the ground state of even-even spherical, axially deformed, triaxially deformed and octupole-deformed nuclei, and give also an example from a calculation with broken time-reversal symmetry. To examine the differences between the convergence of NLO and N2LO Skyrme EDFs, some of these calculations have also been repeated using the SN2LO1 parametrisation of the latter [8] instead.

Four sets of calculations have been performed, using the four possible combinations of gradient descent (GD) and heavy-ball dynamics (HB) for the diagonalisation subproblem and of linear mixing (LM) of the densities and a preconditioned mixing of the potentials (PP) for the SCF subproblem. These are labelled by combinations of letters, from GD+LM to HB+PP.

The parameters dt and α^R entering GD and LM, respectively, have not been optimized, but kept at time-tested values [10, 12] in order to present an accurate image of the methods used in the past. Of course dt is set to a different value for each choice of mesh parameters. For linear mixing, we have fixed $\alpha^R = 0.25$ in Eq. (90) for all densities and no mixing for the potentials. For the HB scheme, we have used the dynamically estimated values from Eqs. (74) and (76). For PP, we have set $\beta^F = 1.0$ in Eq. (95) for F_q^{ρ} and F_q^s as a default value, while not preconditioning any of the other potentials.

All calculations have been initialized with spherical Nilsson orbitals, unless explicitly stated otherwise. For deformed systems, in order to break the spherical self-consistent symmetry, a constraint on the quadrupole moment has been introduced during the first ten iterations in order to break the self-consistent spherical symmetry. In the case of HF+BCS and HFB calculations, we have added a pairing interaction as described in Appendix A.

5.2 Convergence indicators

Several quantities can be used to determine the convergence and its rate for a self-consistent calculation. We will mainly use the ones discussed earlier in Ref. [12]. For convenience, we recall here their definition.

The weighted dispersion of the single-particle energies as a convergence indicator for the linear subproblem has already been introduced in Eq. (65). As we iterate the diagonalisation subproblem only once for every SCF iteration, we will drop the second iteration index in what follows, denoting it $(dh^2)^{(i)}$.

The difference between the total energy calculated from the EDF (1) and from the sum of the occupation-weighted diagonal matrix elements of the single-particle Hamiltonian $\hat{h}^{(i)}$ corrected for rearrangement and pairing energies (see Ref. [12] for the precise definition) also provides a test of convergence of self-consistent calculations. At convergence, when the single-particle Hamiltonian is diagonal, these quantities are equal up to numerical inaccuracies. The difference between the two ways of determining the total energy of the nucleus

$$\delta E_{\text{spwf}}^{(i)} = |E_{\text{func}}^{(i)} - E_{\text{spwf}}^{(i)}|, \quad (98)$$

can then be used as an indicator of convergence. Both $(dh^2)^{(i)}$ and $\delta E_{\text{spwf}}^{(i)}$ cannot become arbitrarily small during the iterative process. The mesh discretization introduces a lower bound for both quantities, that in general decreases when using smaller values of dx [12].

Another indicator that we use in our analysis of convergence is the evolution of the relative change of the total binding energy $\delta E^{(i)}$ from one iteration to the next

$$\delta E^{(i)} = \left| \frac{E^{(i)} - E^{(i-1)}}{E^{(i)}} \right|. \quad (99)$$

As the iterations progress, the change in energy should decrease, and keep decreasing until the limits set by machine precision are encountered. While a large value of $\delta E^{(i)}$ signals non-convergence, we emphasize that a small value does not always signal near-convergence.

5.3 Multipole deformations and multipole constraints

As argued in Section 2.4, we limit the use of constraints in this study to the minimum possible. All algorithms discussed here can easily accommodate their presence. As constraints introduce additional auxiliary conditions to the self-consistent problem that have to be satisfied through an iterative process that has its own convergence rate, they do however unnecessarily complicate the performance comparison of the algorithms discussed here. The discussion of the efficient algorithmic treatment of constraints in the context of the methods used here is deferred to a forthcoming paper [65]. Some of the calculations described in this Section, however, necessitate constraints, such that a few comments on their present implementation are in order.

Generally speaking, constraints on the expectation value of an operator \hat{O} can be imposed by adding a penalty function to the energy. In the case of a single constraint, the single-particle Hamiltonian at the iteration (i) becomes

$$\hat{h}_R^{(i)} = \hat{h}^{(i)} - \lambda^{(i)} \hat{O}, \quad (100)$$

	$N_x = N_y = N_z$	dx (fm)	dt (10^{-22} s)
(a)	32	1.0	0.015
(b)	40	0.8	0.012
(c)	50	0.6	0.006
(d)	64	0.5	0.004

Table 1. Number of mesh points N_μ and mesh spacing dx for the cubic meshes used to calculate the spherical nuclei. The size of the time-step dt for the calculations employing gradient descent is also given.

where $\lambda^{(i)}$ is a Lagrange multiplier. There are two primary possibilities to implement constraints: either keeping the Lagrange parameter λ fixed, in which case the code converges to a configuration with $dE/d\langle\hat{O}\rangle = \lambda$, or adjusting the $\lambda^{(i)}$ during the iterations in such a way that the N -body expectation value $\langle\hat{O}\rangle$ takes a preset value at convergence.

We will use both. For constraints on multipole moments of the mass density, the Lagrange parameters are adjusted with a method similar to the one described in Ref. [12] until a targeted value for the expectation value of $\hat{Q}_{\ell m} \equiv r^\ell Y_{\ell m}(\mathbf{r})$ is reached. To plot results, however, we will use the dimensionless deformations [12]

$$\beta_{\ell m} = \frac{4\pi}{3R^\ell A} \langle\hat{Q}_{\ell m}\rangle \quad (101)$$

instead, where $R = 1.2A^{1/3}$ fm. For systems with triaxial quadrupole deformation, we use the quantities [12]

$$\beta \equiv \sqrt{\beta_{20}^2 + 2\beta_{22}^2}, \quad \gamma \equiv \text{atan2}(\sqrt{2}\beta_{22}, \beta_{20}), \quad (102)$$

to draw maps in the β - γ plane. The multipole constraints are mainly used to provide background energy surfaces that illustrate the path of the evolution of unconstrained calculations towards the minimum. An exception are some calculations with broken reflection symmetry, where a constraint on the position of the centre-of-mass of the nucleus has to be added in order to keep the system fixed at the centre of the numerical box.

5.4 Spherical nuclei

First tests have been performed for the spherical nuclei ^{40}Ca , ^{132}Sn and ^{208}Pb using the NLO and N2LO functionals. The mesh discretization dx has been varied according to Table 1. As shown in [2], mesh (b) offers an satisfactory compromise between numerical accuracy and CPU time for nuclei up to ^{208}Pb .

Figure 10 shows the evolution of the relative change in total energy $\delta E^{(i)}$ and the weighted dispersion $(dh^2)^{(i)}$ as a function of the number of iterations for the three nuclei and the two parametrisations. Results obtained with a given combination of algorithms are very similar for all parametrisations and nuclei. The combination GD+LM is always the least favourable while HB+PP is the fastest.

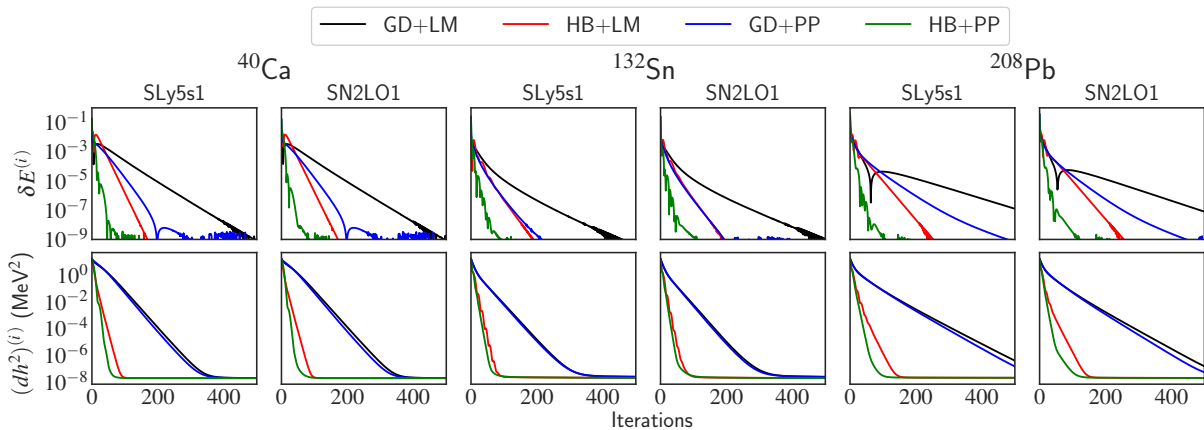


Fig. 10. Comparison between four combinations of algorithms for the spherical nuclei ^{40}Ca , ^{132}Sn and ^{208}Pb for the SLy5s1 (left) and the SN2LO1 functionals (right), calculated without pairing correlations on mesh (b).

It is important to realize that different indicators are sensitive to different aspects of the convergence. This can be most clearly seen when looking at results from the HB+LM and GD+PP schemes that give intermediate results. For HB+LM, the weighted dispersion $(dh^2)^{(i)}$ always falls off much quicker than $\delta E^{(i)}$. This indicates that in this case the late stages of the convergence are dominated by small changes of the densities and potentials in the SCF iteration, while the single-particle Hamiltonian $\hat{h}^{(i)}$ is already near-diagonal and rediagonalised with a single step of the HB scheme after each SCF update. When combining HB with PP, then both aspects converge at a similar rapid pace. For GD+PP one finds the opposite of HB+LM: $\delta E^{(i)}$ falls off quicker than $(dh^2)^{(i)}$. In this case, the late stages of the convergence are dominated by the diagonalisation subproblem, while thanks to the preconditioner the potentials and densities are already near the self-consistent solution for the given set of single-particle states $\{|\psi_\ell^{(i)}\rangle\}$ and can be made to follow its slow evolution with a single preconditioned update. In that respect, HB+PP and GD+LM are similar as in both schemes the two subproblems converge at a similar rate.

Figure 10 illustrates that one cannot rely on a single quantity like $\delta E^{(i)}$ as an indicator of convergence, as different indicators probe different aspects of the convergence of the self-consistent problem. As already discussed in Section 3, the convergence rate depends on the representation, as do the smallest values reachable for the indicators. This is illustrated by Fig. 11, which shows the evolution of the weighted dispersion $(dh^2)^{(i)}$ and of $\delta E_{\text{spwf}}^{(i)}$ for a HB+PP calculation of the spherical ground state of ^{40}Ca and the four different mesh discretizations dx as indicated in Table 1. In general, both indicators reach a plateau that originates from calculating the energy from the single-particle states through different intermediate objects that are not equally resolved on a given mesh. The smaller the value of dx , the lower this plateau, although there is also a lower limit to these plateaus that is set by the level of truncation and round-off errors of floating-point arithmetic. For $(dh^2)^{(i)}$, this limit is reached

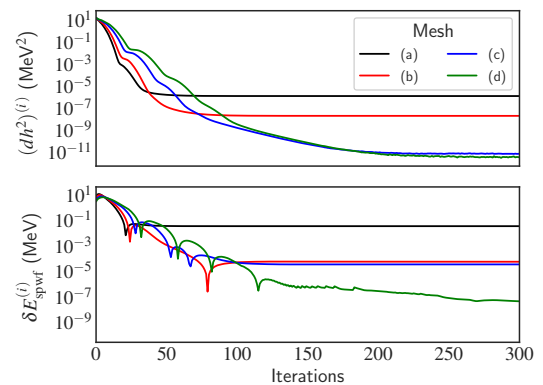


Fig. 11. Weighted dispersion (top) and $\delta E_{\text{spwf}}^{(i)}$ (bottom) as a function of the iterations for the various mesh choices of Table 1 and a HF calculation of ^{40}Ca using the HB+PP scheme and the SLy5s1 parametrisation.

for mesh (c). Both quantities probe the quality of the diagonalisation of $\hat{h}^{(i)}$, and, hence, behave in roughly the

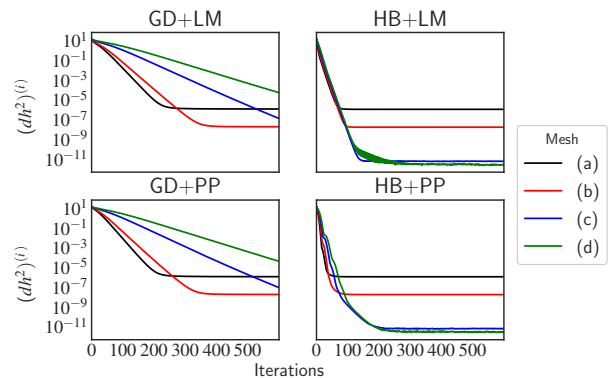


Fig. 12. Weighted dispersion (top) as a function of the iterations for the various mesh choices of Table 1 and a HF calculation of ^{40}Ca with the schemes as indicated and the SLy5s1 parametrisation.

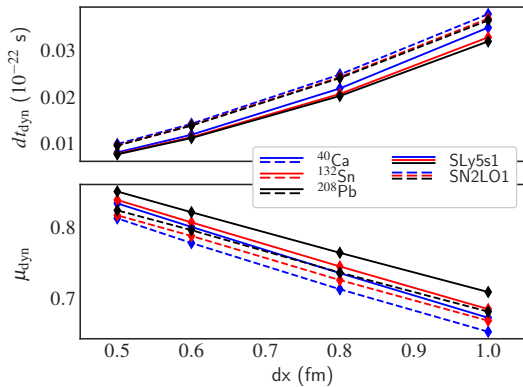


Fig. 13. Iterative parameters dt_{dyn} and μ_{dyn} at the end of the iterative process, as estimated by Eqs. (74) and (76), for ^{40}Ca (blue), ^{132}Sn (red) and ^{208}Pb (black) using the SLy5s1 (full lines) and SN2LO1 (dashed lines) parametrizations.

same way, with the plateau reached at about the same iteration number. Since these quantities are interchangeable for the purpose of our analysis, we focus on the weighted dispersion.

As already discussed for Fig. 4, the number of iterations needed to reach the same level of convergence in the HB scheme is almost independent of dx , while in the GD method it increases dramatically with decreasing dx . Figure 12 illustrates this for the convergence of the weighted dispersion $(dh^2)^{(i)}$ during a calculation of ^{40}Ca with the four different schemes. The schemes employing HB are clearly superior for meshes with small dx , in particular when recalling that each individual iteration becomes much more costly when reducing dx . Interestingly, the convergence of the HB+LM scheme shows almost no dx dependence apart from reaching different plateau levels. By contrast, the speed-up from the pre-conditioner when going from HB+LM to HB+PP re-introduces a very small dx dependence, albeit on a much weaker level than what is observed for LM schemes.

A large part of the levelling out of the dx dependence of convergence when using the HB scheme is made possible by the dynamical adaptation of its numerical parameters, as already discussed in Section 3.6. Figure 13 shows the values of the parameters μ_{dyn} and dt_{dyn} of the HB scheme calculated from Eqs. (74) and (76) at the last iteration of the HB calculations displayed in Fig. 12. For a given mesh discretization, the value of dt_{dyn} is almost twice as large as the largest value that can safely be used in gradient descent. While the time-step dt_{dyn} shrinks with decreasing dx , its negative effect on the convergence rate is counterbalanced by an increase of the parameter μ_{dyn} , reflecting an increasing mismatch between the smallest and largest relevant energy scale.

5.5 Deformed nuclei

Let us now compare the convergence properties of the four methods that we have defined for three deformed nuclei

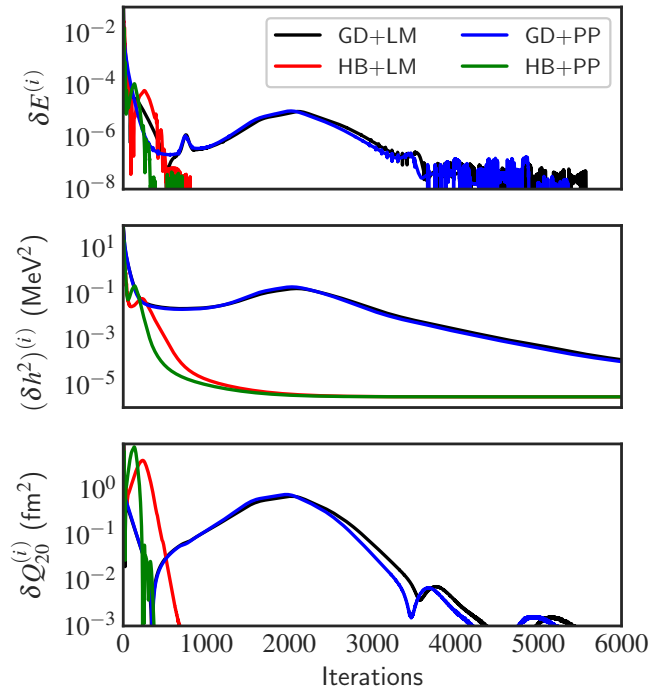


Fig. 14. Evolution of the change in energy (top), weighted dispersion (middle) and change in axial quadrupole moment (bottom) as a function of iterations for ^{240}Pu using the SLy5s1 parametrization.

with qualitatively different energy surfaces when initialized at a deformation far from the one of the ground state. In all cases, the mesh-choice (b) from Table 1 has been used together with the SLy5s1 parametrization. All calculations consider pairing correlations in order to allow for a smooth evolution of the deformation.

As a first example we address the axially-deformed ground state of ^{240}Pu . For this parametrization, it takes a quadrupole deformation of $\beta_{20} \simeq 0.28$ that is accompanied by an energy gain of about 15 MeV compared to the spherical configuration [64]. Figure 14 shows the evolution of the relative change in energy $\delta E^{(i)}$, the weighted dispersion $(dh^2)^{(i)}$, and the change of quadrupole moment $\delta Q_{20}^{(i)} \equiv |Q_{20}^{(i)} - Q_{20}^{(i-1)}|$, during the iteration.

The algorithms including heavy-ball dynamics are again by far superior to those based on gradient descent. They provide a reduction in the number of iterations of about one order of magnitude. The main source for this gain is the much quicker convergence of the deformation, in particular when combining heavy-ball dynamics with the potential preconditioner, which reduces the number of iterations needed to bring the deformation close to the converged value by again a factor of two. This then also accelerates the final convergence of the potentials in the SCF problem.

The reduction in number of iterations brought by the HB scheme compared to the GD method is even more remarkable when searching for the minimum of a deformation energy surface that is soft in one direction. As an

example we choose ^{64}Ge . To illustrate the advancement of the calculation of the ground state, we have first determined the (converged) deformation energy surface of this nucleus as a function of β and γ . Its ground state is triaxial with $\beta \simeq 0.25$ and $\gamma = 27^\circ$. We have then performed unconstrained calculations of the ground state with the four methods that we study. Each calculation is initialized with a configuration that has been pushed away from the spherical point by applying a constraint on a slightly triaxial quadrupole moment for 10 iterations. The paths followed during the iterations are indicated by dashed lines in Fig. 15, with additional markers at every 100 iterations. During the initial constrained phase of the calculation, the state is pushed to $\beta \simeq 0.28$ at $\gamma \simeq 2.4^\circ$, i.e. the end of the straight part of the dashed line. When the constraint is released, all calculations go back to smaller values of β at almost constant γ . What happens after depends on the scheme. The methods containing GD go back to much smaller $\beta \simeq 0.12$ within about 200 iterations, before starting to go downhill to larger β again for a second time. By contrast, the methods containing the HB scheme only go back to the bottom of the valley and then turn directly to larger γ angles.

The difference between HB and GD is that during the SCF iterations the former arrives so quickly at an approximate diagonalisation of $\hat{h}^{(i)}$ that the SCF iteration actually moves on an energy surface that is quite close to the converged energy surface drawn as the background in Fig. 15 and therefore can follow the valleys seen in the plot. By contrast, the GD scheme remains for the first few hundred iterations so far from the diagonalisation of $\hat{h}^{(i)}$

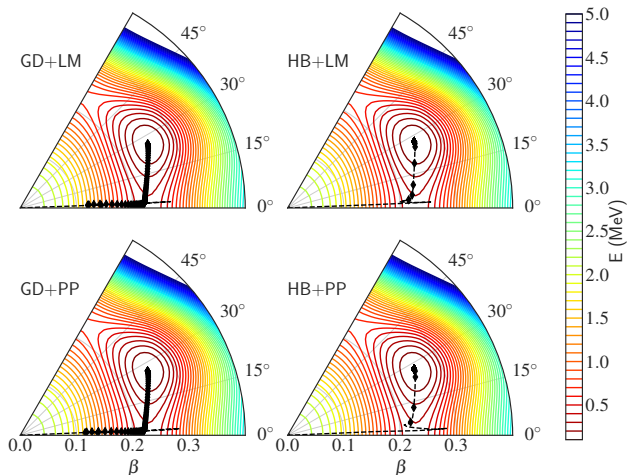


Fig. 15. Quadrupole deformation β and triaxiality angle γ as a function of the iterations of a non-constrained calculation of ^{64}Ge with the four algorithms as indicated, drawn against a backdrop of the converged deformation energy surface. Contour lines are at every 100 keV and diamonds at every 100th iteration. Calculations were initialized with the (converged) spherical configuration pushed with a constraint to slightly non-axial quadrupole deformation for 10 iterations (see text).

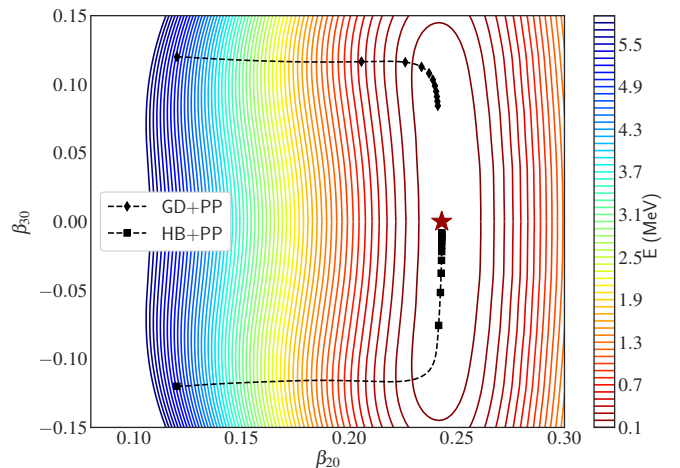


Fig. 16. Path in the (β_{20}, β_{30}) plane of a calculation for ^{232}Th initialized at $\beta_{20} = |\beta_{30}| = 0.12$ using the SLy5s1 parametrisation, and employing gradient descent (diamonds) or heavy-ball dynamics (squares). The HB path is drawn at negative β_{30} for ease of presentation, but is physically equivalent. Markers are placed at initialization and at every 500th iteration, with the final point placed after 5000 iterations. Both approaches employed potential preconditioning. The contour lines are 100 keV apart, while the minimum of the energy surface at $\beta_{30} = 0.0$ is indicated by a red star.

that during this phase the SCF evolution is on a very different energy landscape, in which the valley visible in the converged energy surface of Fig. 15 emerges only slowly during the iterative process. This is corroborated by the number of iterations needed in each scheme to reach the turn-off point where the evolution turns into the direction of γ . The GD+LM scheme needs 3990 iterations to reach that point, while for GD+PP it are 3702. This has to be contrasted with 22 iterations needed for HB+LM and just 17 for HB+PP. But also for the latter two schemes finding the minimum in the soft γ direction requires many more iterations than finding the valley in the steep β direction. The HB+PP scheme arrives at the minimum after about 700 iterations, while it takes about 900 for HB+LM, and around 10000 for GD+LM and GD+PP. For this kind of calculation, HB dynamics is clearly superior to GD, with PP performing slightly better than LM.

As a final example of the calculation of deformed ground states, we have selected ^{232}Th , a nucleus with an axial reflection-symmetric quadrupole deformed ground state that is very soft with respect to octupole degrees of freedom [64]. At the quadrupole deformation of the minimum, the energy varies by less than 100 keV over a wide range of β_{30} values up to 0.14. As in the previous case, we have first calculated the (β_{20}, β_{30}) energy surface in order to have a background for the analysis of the evolution of the non-constrained calculation. As in the case of ^{64}Ge , the difference between using the LM or PP scheme is minimal compared to the difference between using GD and HB, such that we will limit the presentation to the HB+PP and GD+PP combinations. Profiting from the symmetry of the deformation energy when reversing the sign of β_{30} ,

Fig. 16 displays the evolution of the GD+PP calculation at positive β_{30} , whereas results for HB+PP are drawn at negative β_{30} . The calculations were both run for 5000 iterations, initialized from the same converged state constrained to $\beta_{20} = \beta_{30} = 0.12$. They follow the paths indicated by the dashed line, with additional markers set at every 500 iterations. As the calculations are this time started from a converged state on the slope of the energy surface, they explore almost the same energy surface during the calculation, optimizing again first the energy in steep directions of the surface, which is β_{20} , and then slowly follow the tiny gradient in the soft direction. This admittedly pathological example is a challenge not only because of the energy surface being flat, but also because convergence requires the state to adopt a higher symmetry than the one the calculation is initialised with. After 5000 iterations, the heavy-ball scheme almost arrives at the minimum, while gradient descent is still very far from it. The latter, however, cannot be guessed from the convergence indicators, which at the 5000th iteration take the values $\delta E^{(i)} = 3 \times 10^{-9}$ MeV, $(dh^2)^{(i)} = 4 \times 10^{-7}$ MeV², and $\delta Q_{30}^{(i)} \equiv |Q_{30}^{(i)} - Q_{30}^{(i-1)}| = 6 \times 10^{-6}$ fm³.

When organising self-consistent calculations, some of the issues of slow convergence of deformation degrees of freedom discussed here can to some extent be compensated for by using prior information about the structure of the energy surface by initialising a calculation from a reasonably converged calculation that has been constrained to a shape similar to the one of the targeted configuration. Such procedure, however, requires human time to prepare calculations according to the targeted nucleus or even parametrisation. An algorithm like HB+PP that homes in quickly on the ground state after just having been pushed into roughly the right direction, as in the case of the example of ⁶⁴Ge, brings not just a large reduction of computational time, but also in human time needed to prepare, run, and survey the calculations.

5.6 Cranked calculations

At the mean-field level, rotational bands can be described through the introduction of a cranking constraint [20, 66]. In many cases, it is sufficient to constrain one component of angular momentum \hat{J}_z , such that the mean field entering the HFB Hamiltonian (4) is replaced by

$$\hat{h}_C^{(i)} = \hat{h}^{(i)} - \omega \hat{J}_z. \quad (103)$$

The rotational frequency ω plays the role of a Lagrange multiplier. The calculations reported here are performed at fixed values of ω , such that the constraint acts as an external potential that does not change during the iterations.

For the calculations discussed so far, time-reversal invariance can be imposed on the product state, which can be used to simplify the calculations. The cranking constraint in Eq. (103) breaks time-reversal invariance, such that one has to consider also time-odd densities, the time-odd terms in the EDF, Eqs. (19) and (20), and the corresponding terms in the single-particle Hamiltonian, Eq. (29).

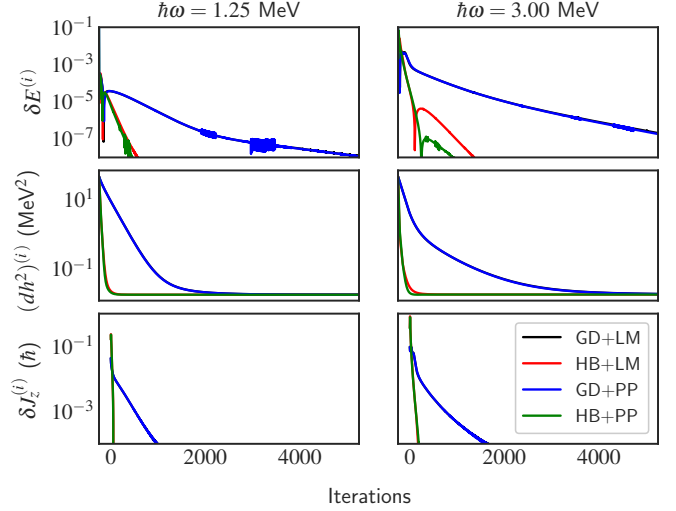


Fig. 17. Evolution of the relative change in total energy (top), weighted dispersion of the single-particle Hamiltonian (middle), and change in expectation of angular momentum $\langle J_z \rangle$ (bottom) for cranked calculations of ²⁴Mg at $\hbar\omega = 1.25$ MeV (left) and $\hbar\omega = 3.00$ MeV (right) using the SLy5s1 parametrisation.

We note in passing that the SLy5s1 parametrisation that we use here has been constructed such that it does not have an unphysical finite-size instability in the time-odd terms, a problem encountered for many other parametrisations of the Skyrme EDF [26].

The light deformed nucleus ²⁴Mg is a popular testing ground for the modelling of rotational bands. Figure 17 shows the evolution of $\delta E^{(i)}$, $(dh^2)^{(i)}$, and the change in angular momentum

$$\delta J_z^{(i)} = |\hat{J}_z^{(i)} - \hat{J}_z^{(i-1)}|, \quad (104)$$

during the iterations for two different values of the cranking frequency ω . The non-cranked HFB ground-state is prolate and time-reversal invariant. It has been used to initialize all calculations. To avoid the breakdown of pairing correlations, the HFB method is supplemented by the Lipkin-Nogami procedure [37].

As for non-cranked calculations, combinations of algorithms using heavy-ball dynamics significantly outperform combinations with gradient descent, with a reduction of the necessary number of iterations necessary to reach similar quality by almost one order of magnitude. The difference between the HB and GD schemes is especially visible for the angular momentum: it converges in a few iterations with heavy-ball dynamics, but requires three orders of magnitude more iterations with gradient descent. Similarly, $(dh^2)^{(i)}$ falls to the plateau value much quicker when using HB dynamics, indicating that $\hat{h}_C^{(i)}$ is near-diagonal throughout most of the SCF iterations. Although cranked HFB states are necessarily non-axial, in this example the deformation changes only minimally when varying ω in the range covered. For this reason, potential preconditioning does not have a large effect, even though for $\hbar\omega = 3$ MeV a small speed-up is observed in the change in energy.

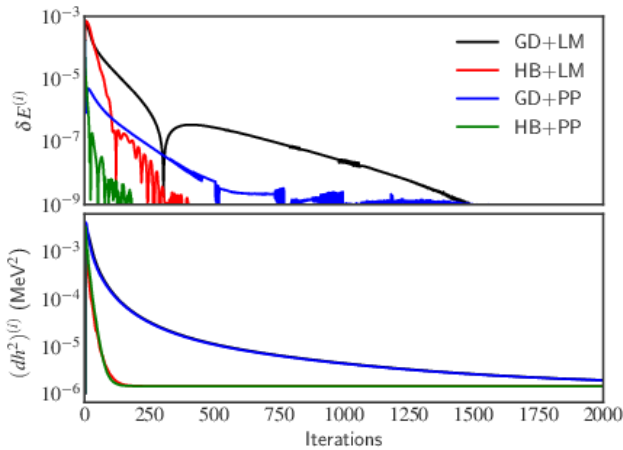


Fig. 18. Evolution of the relative change in total energy (top) and weighted dispersion of the single-particle Hamiltonian (bottom) for a blocked HFB calculation of the $K \approx 9/2^-$ ground state of ^{251}Fm . In the lower panel, the curves for GD+LM and GD+PP are on top of each other.

5.7 Odd-mass nuclei

Within the framework of the two-basis method to solve the HFB equations, all algorithms described above work in exactly the same way for one-quasiparticle states representing odd-mass nuclei as they do for even nuclei. The only difference specific to odd nuclei, or any multi-quasiparticle state for that matter, concerns the construction of the U and V matrices when solving the HFB equation (4) in the subspace provided by the $|\psi_k^{(i)}\rangle$. The tagging of a specific configuration, however, introduces auxiliary conditions that have to be satisfied by the solution of the self-consistent problem. As the analysis of algorithms that follow the targeted configuration through large changes of the single-particle spectrum is out of the scope of this paper, we address only the simple case of a well-deformed odd-mass nucleus that is initialised from a converged false vacuum with same proton and neutron number, and therefore similar deformation. The blocking of a quasiparticle breaks time-reversal invariance with the same consequences as in the case of cranked HFB, and is carried out as described in Ref. [22].

As example, Fig. 18 shows the evolution of $\delta E^{(i)}$ and $(dh^2)^{(i)}$ during the iterations of the near-axial $K \approx 9/2^-$ ground state of ^{251}Fm , calculated in HFB with the NLO SLy5s1 parametrisation. Once again, combinations of algorithms using heavy-ball dynamics outperform combinations with gradient descent, leading to a large reduction of the number of iterations. Very similar to the other cases discussed already, the heavy-ball scheme quickly near-diagonalises $\hat{h}^{(i)}$ for the lowest occupied single-particle states, although $\hat{h}^{(i)}$ continues to be updated for much longer by the SCF iterations. When using the heavy-ball scheme, the preconditioner also visibly reduces the number of necessary SCF iterations compared to linear mixing.

6 Discussion, summary, and conclusions

The self-consistent mean-field equations present a non-linear numerical problem that needs to be solved with iterative methods. Carrying out a calculation such that it converges reliably and efficiently to the targeted nuclear configuration requires the control over many interlocking aspects of the numerical problem. We have discussed here the role of the two most essential components of such a calculation.

The first component is the diagonalisation subproblem: the diagonalisation of the single-particle Hamiltonian for a given set of mean-field potentials. In many cases, iterative diagonalisation algorithms are the most efficient ones when dealing with a large single-particle basis.

The second component is constituted by the SCF iterations, whose goal is to find a fixed point of the mean-field equations for the densities and potentials that determine the single-particle Hamiltonian. This component always requires an iterative approach.

For both components, the design of the iterative process algorithms has to take into consideration that there are “soft” and “stiff” directions in the solution space. The most problematic for the stability of the numerical solution are highly oscillatory modes: already a tiny accidental admixture of such modes during the updates of either the single-particle states or the potentials can excite the system and drive it away from convergence. For the Skyrme EDF, the degrees of freedom that dominate such behaviour in the diagonalisation subproblem on the one hand and the SCF iteration on the other hand can be easily identified. The former is connected to terms with external gradients of the local densities in Eqs. (18), (20), and (22), whereas the latter is connected to the number of gradients contained in the local densities defined through Eqs. (12) and (13). For finite-range interactions, the inadequate treatment of large eigenvalues of the single-particle Hamiltonian or of a large Jacobian of the SCF iteration will lead to the same convergence problems. For such types of EDF, however, the dominant terms that contribute to each are not straightforward to identify, in particular when keeping the exact exchange terms.

In practice, the presence of these problems results in the need to select one or even several numerical parameters such that numerical instabilities are avoided, with the side-effect of slowing down overall convergence. The feasible (and optimal) values of these parameters depend in general on the numerical representation, the range of resolved momenta, the properties of the parametrisation of the EDF used in a calculation, and sometimes even on the nucleus. Therefore, the numerical parameters have either to be adapted case by case or to be fixed on the safe side which translates into human cost in the first case and in increase of CPU time in the second case.

We have discussed three distinct aspects of the convergence of self-consistent calculations with Skyrme EDFs in this study, which can be summarised as follows.

Parametrisation dependence of the diagonalisation subproblem. The problematic degrees of freedom for the diagonalisation subproblem are related to the largest eigenvalues of the single-particle Hamiltonian, which correspond to highly oscillatory single-particle wave functions. Proceeding too quickly in the iterative diagonalisation can have the side-effect of unintentionally amplifying (instead of damping) these oscillations.

For a Skyrme EDF, the coupling to such states is determined by the internal gradients present in the local densities out of which the functional is built. For NLO parametrisations with realistic effective masses in the four spin-isospin channels the kinetic energy is always the leading term in that respect.

The Skyrme EDF at N2LO yields additional contributions, some of which scale differently because of their higher number of internal gradients such as the density $Q(\mathbf{r})$ of Eq. (13). There is no a priori about the relative sign of coupling constants of the additional terms, which leads to a complicated interplay between terms that, depending on the parametrisation, might either reduce or amplify the coupling to oscillatory modes compared to the NLO case.

Parametrisation dependence of the SCF subproblem.

The algorithm for SCF iteration might inadvertently amplify oscillatory modes of the densities and mean-field potentials. By linearising the evolution, this behaviour can be directly related to the largest eigenvalues of the Jacobians of the SCF evolution.

For a Skyrme EDF, these problematic eigenvalues are largely determined by the presence of external derivatives of local densities in the EDF. For most parametrisations at NLO, the isoscalar $\rho_0(\mathbf{r})\Delta\rho_0(\mathbf{r})$ term dominates the evolution of the SCF iteration, as among the contributions to the potentials with two external gradients it is the one with largest coupling constant. As this term provides a dominant contribution to the surface tension [64], for realistic parametrisations its coupling constant is always of the same sign and takes very similar values. This is different for the homologues of this term in the other spin-isospin channels that often vary over a large range, which can result in the need to fine-tune numerical parameters.

At N2LO there are again additional terms containing gradients of densities, some of which concern other potentials, and some of which have a different scaling because of their higher number of external gradients, an example being the $\rho(\mathbf{r})\Delta\Delta\rho(\mathbf{r})$ term in Eq. (22). Again, there is no a priori about the relative sign of the coupling constants of the new terms, which again might require a case-by-case fine-tuning of numerical parameters of the SCF iteration.

These convergence problems have to be distinguished from finite-size instabilities of the parametrisations of the EDF as discussed in Refs. [26, 52, 53, 54]. Although their effect on the progression of an iterative calculation is the same, i.e. they trigger oscillations that grow larger at each iteration, their origin is different: the numerical instability discussed here results from the unintended coupling to oscillatory modes that are less bound. By contrast, a finite-

size instability of a given parametrisation results from states with a highly oscillatory density distribution being more bound than states with a physical density distribution. The former can be avoided with a suitable choice of numerical parameters, whereas the latter is a physical attribute of a parametrisation that might, however, not always be well resolved by a given numerical representation [52].

Algorithmic improvements. We have discussed two often-used methods, gradient descent and linear density mixing and their limitations with respect to the treatment of the problematic oscillatory modes in both the diagonalisation and SCF subproblems. To alleviate said limitations, we have proposed two algorithmic improvements, heavy-ball dynamics and potential preconditioning, which have several major advantages.

Compared to the gradient-descent approach, the heavy-ball algorithm, requires significantly less iterations in all cases we have investigated so far, and this at a negligible increase of numerical cost of each iteration. The improvement is especially striking when the energy surface is soft around the targeted configuration, or when very large eigenvalues of the single-particle Hamiltonian are present. In a coordinate-space representation, the heavy-ball method removes the inverse scaling of the number of total iterations with the mesh parameter that otherwise leads to a disproportionate increase of computational cost when reducing dx .

In spite of their large difference in performance, the implementation of the heavy-ball method differs only little from the gradient-descent approach and can be easily implemented into existing solvers using that method. In the context of self-consistent mean-field calculations, the number of additional operations and the size of additional storage space are negligible compared to what is already needed for the more basic gradient descent.

The second algorithmic improvement concerns the SCF iteration. Instead of indiscriminately damping changes at all wavelengths, we propose a preconditioning scheme for the mean-field potentials that permits for more rapid updates of long-wavelength changes compared to short-wavelength ones. This selective damping especially improves the convergence of calculations for deformed nuclei, as deformation can be allowed to changed more rapidly while maintaining the stability of the calculation. As for heavy-ball dynamics, the method is straightforward to implement into existing solvers employing linear mixing. Although the preconditioning step demands significantly more CPU operations than linear mixing, its impact on overall CPU time is negligible, as the cost of the diagonalisation subproblem remains the dominant one.

Finally, we propose a dynamical estimate of the optimal numerical parameters for both gradient-descent and heavy-ball dynamics. Also, it turns out that for existing parametrisations of the Skyrme EDF the performance of potential preconditioning for the SCF subproblem is not sensitive to the choice numerical parameters. In this way,

human fine-tuning of parameters is no longer necessary in virtually all cases, without sacrificing CPU time.

Outlook. The better understanding of the limiting factors of the diagonalisation and SCF subproblems allowed us to propose algorithmic improvements that result in a reduction of needed CPU time that often reach a factor of ten, as well as an almost complete elimination of the need for fine-tuning the numerical parameters. These advances can now be exploited to perform systematic calculations across the nuclear chart at a significantly reduced cost, both in terms of CPU and human time. This improvement is particularly welcome for the exploration of the possibilities of future N2LO parametrisations, for which the performance of gradient descent and linear mixing can change dramatically as a result of small modifications of the coupling constants.

More specifically, with these improvements CPU-intensive calculations with our MOCCa code that simultaneously break multiple point-group symmetries can now be performed on a large scale, especially for systems whose energy surface is very soft in one shape degree of freedom. This opens the way for future systematic investigations of rotational bands based on exotic nuclear configurations.

Acknowledgements

The majority of calculations have been performed at the Computing Centre of the IN2P3. Another significant part of computational resources have been provided by the Consortium des Équipements de Calcul Intensif (CÉCI), funded by the Fonds de la Recherche Scientifique de Belgique (F.R.S.–FNRS) under Grant No. 2.5020.11.

A The two-basis method for HFB calculations in coordinate space

Most implementations of the HFB equations represent Eq. (5) as a $2N_b \times 2N_b$ diagonalisation problem in the numerical single-particle basis, where the quasi-particle states $(U_\mu V_\mu)^T$ are given by the columns of the sub-matrices of the Bogoliubov transformation [20]

$$\beta_\mu = \sum_{j=1}^{N_b} (U_{j\mu}^* a_j + V_{j\mu}^* a_j^\dagger) \quad \text{for } \mu = 1, \dots, N_b. \quad (105)$$

Instead of diagonalising the HFB Hamiltonian in the numerical basis, it can also be diagonalised in the single-particle basis $|\psi_j\rangle$ that diagonalises the single-particle Hamiltonian

$$\hat{h}|\psi_j\rangle = \epsilon_j |\psi_j\rangle, \quad (106)$$

with eigenvalues ϵ_j that are usually called single-particle energies. The HF basis is obtained from the numerical

basis by the unitary transformation $CC^\dagger = C^\dagger C = 1$ that diagonalises the single-particle Hamiltonian

$$C^\dagger h C = \epsilon, \quad (107)$$

where ϵ is the diagonal matrix with the single-particle energies as entries. In the basis of the eigenstates of the single-particle Hamiltonian, the HFB matrix takes the form

$$\tilde{\mathcal{H}} \begin{pmatrix} \tilde{U}_\mu \\ \tilde{V}_\mu \end{pmatrix} = \begin{pmatrix} \epsilon - \lambda & \tilde{\Delta} \\ -\tilde{\Delta}^* & -\epsilon + \lambda \end{pmatrix} \begin{pmatrix} \tilde{U}_\mu \\ \tilde{V}_\mu \end{pmatrix} = E_\mu \begin{pmatrix} \tilde{U}_\mu \\ \tilde{V}_\mu \end{pmatrix} \quad (108)$$

where the tilde in $\tilde{\mathcal{H}}$ and $\tilde{\Delta}$ indicates that these matrices are now calculated in the HF basis. The diagonalisation of \hat{h} and $\tilde{\mathcal{H}}$ are of course interlaced, as the density matrix in the HF basis $\rho_{jk} = (\tilde{V}^* \tilde{V}^T)_{jk}$ enters the calculation of the densities that determine \hat{h} .

Originally proposed in Ref. [22], the two-basis method consists of determining the quasi-particle basis that diagonalises \mathcal{H} in terms of the HF basis. It has been used in 3d coordinate-space calculations since [22, 67, 64]. It has also been implemented into the 1d spherical coordinate-space HFB solver LENTEUR [36] and the 3d HO code HFODD [68], in both cases with an exact diagonalisation of \hat{h} at each self-consistent field iteration.

Up to this point we just performed a basis transformation. When introducing an effective pairing interaction with a suitably chosen cutoff f_ℓ that in the HF basis is a function of the distance $(\lambda - \epsilon_\ell)$ of the single-particle energy ϵ_ℓ from the Fermi energy λ , the pairing energy E_{pair} and pairing gaps $\tilde{\Delta}_{ij}$ become

$$E_{\text{pair}} = \frac{1}{2} \sum_{ijkl} f_i f_j f_k f_l \tilde{v}_{ijkl} \tilde{\kappa}_{ij}^* \tilde{\kappa}_{kl}, \quad (109)$$

$$\tilde{\Delta}_{ij} = f_i f_j \frac{1}{2} \sum_{kl} f_k f_l \tilde{v}_{ijkl} \tilde{\kappa}_{kl}, \quad (110)$$

where \tilde{v}_{ijkl} , $\tilde{\kappa}_{ij}^*$ and $\tilde{\kappa}_{kl}$ are now also calculated in the HF basis. With such a cutoff, single-particle states above the pairing window have an occupation zero, such that the elements³ $\tilde{\rho}_{jk} = (\tilde{V}^* \tilde{V}^T)_{jk}$ and $\tilde{\kappa}_{jk} = (\tilde{V}^* \tilde{U}^T)_{jk}$ of the normal and anomalous density matrices that multiply their contribution to many-body observables are zero. For these states, $\tilde{\mathcal{H}}$ is already diagonal, as the corresponding matrix elements in $\tilde{\Delta}$ are also zero. It is therefore sufficient to limit the quasiparticle basis to Ω states

$$\beta_\mu = \sum_{j=1}^{\Omega} (\tilde{U}_{j\mu}^* c_j + \tilde{V}_{j\mu}^* c_j^\dagger) \quad \text{for } \mu = 1, \dots, \Omega, \quad (111)$$

where \tilde{U} and \tilde{V} are the submatrices of the Bogoliubov transformation between the HF basis and the HFB basis and Ω is the size of a set of single-particle states in the HF basis chosen large enough that it encompasses those

³ Note that in our notation $\tilde{\rho}$ is the normal density matrix in the HF basis. Many papers use $\tilde{\rho}$ for a pair density matrix instead.

for which matrix elements $\tilde{V}_{j\mu}$ are non-zero. With this, one has mapped the HFB problem from the diagonalisation of a $2N_b \times 2N_b$ problem to two coupled problems of much smaller dimension.

In the calculations presented here, we have systematically employed the pairing interaction as proposed in Ref. [37] with a cutoff of 5 MeV above and below the Fermi energy.

B The link with the damped harmonic oscillator

We briefly show the link between the heavy-ball dynamics equations and the equations of the damped harmonics oscillator. For a more in-depth analysis, we refer the reader to Ref. [44].

The classical equation of motion of a one-dimensional damped harmonic oscillator with coordinate $x(t)$ is given by

$$m \frac{d^2 x(t)}{dt^2} + M \frac{dx(t)}{dt} + \omega^2 x(t) = 0. \quad (112)$$

where m is the mass and ω the oscillator frequency, while M is a constant that governs the friction applied to the oscillator. In order to numerically integrate the equation of motion (112), it has to be discretized. In terms of a (small) step size δt and an auxiliary variable $V(t)$, we have

$$\begin{cases} V(t + \delta t) = \frac{m\delta t}{(m + M\delta t)} V(t) - \frac{\delta t^2 \omega^2}{(m + M\delta t)} x(t), \\ V(t) = x(t + \delta t) - x(t), \end{cases} \quad (113)$$

Making a further change of variables

$$\mu = \frac{m\delta t}{(m + M\delta t)}, \quad \Omega^2 = \frac{\delta t \omega^2}{(m + M\delta t)}, \quad (114)$$

and rearranging both equations, we obtain

$$\begin{cases} x(t + \delta t) = x(t) + V(t + \delta t), \\ V(t + \delta t) = -\delta t \Omega^2 x(t) + \mu V(t). \end{cases} \quad (115)$$

Given appropriate initial conditions, this coupled set of equations can be integrated. It is identical to Eq. (57), with the iteration count taking the role of discrete time, the stepsize α taking the role of δt , and the eigenvalue λ_k figuring as the square of the (modified) oscillator frequency Ω^2 .

Let us classify the various solutions of Eq. (112) for an oscillator starting from $x(0) = x_0$, with $V(0) = 0$. One can verify that the following prescription

$$x(t) = \frac{x_0}{2} e^{-\gamma t} (e^{i\omega_0 t} + e^{-i\omega_0 t}), \quad (116)$$

is a solution to Eq. (112), provided that

$$\gamma = \frac{M}{2m}, \quad \omega_0^2 = \frac{\omega^2}{m} - \frac{M^2}{4m^2}. \quad (117)$$

We differentiate three different regimes, depending on the value of ω_0^2

$$\begin{cases} \omega_0^2 > 0 \text{ underdamped,} \\ \omega_0^2 = 0 \text{ critically damped,} \\ \omega_0^2 < 0 \text{ overdamped.} \end{cases} \quad (118)$$

When underdamped, $x(t)$ oscillates rapidly around zero with an exponentially decaying amplitude. When overdamped, the system decays exponentially to zero without oscillations. The rate at which it does so is determined by both γ and ω^2 : when ω_0^2 becomes more negative, the system decays increasingly slow. For a critically damped system, the system also does not oscillate around zero, but rather decays directly at a rate of $-\gamma$.

Achieving critical damping should be the goal if we desire a system that decays as rapidly as possible. The condition on the damping M is

$$M_{\text{crit}}^2 = 4m\omega^2. \quad (119)$$

This corresponds in the discrete case to

$$\mu_{\text{crit}} = \left(1 - \sqrt{\delta t \Omega^2}\right) + O(\delta t^2), \quad (120)$$

where we ignore corrections of second order in δt .

The gradient-descent equations can be obtained by simply setting m to 0. The system then is always overdamped and decays only comparatively slowly to $x = 0$.

The discretization of a differential equation cannot be reliably numerically integrated for arbitrary δt , as too large values can lead to unstable integration schemes. This is the direct analogue for differential equations of condition Eq. (71); if Ω^2 is large, then Eq. (112) is a so-called stiff differential equation [40]. For such cases, the numerical integration requires either very small time-steps or more advanced discretization schemes, which is another way of interpreting the upper bound on the stepsizes α and dt discussed in the main text.

References

1. M. Bender, P.-H. Heenen and P.-G. Reinhard, *Self-consistent mean-field models for nuclear structure*, Rev. Mod. Phys. **75**, 121 (2003).
2. W. Ryssens, M. Bender and P.-H. Heenen, *Numerical accuracy of mean-field calculations in coordinate space*, Phys. Rev. C **92**, 064318 (2015).
3. A. Arzhanov, T. R. Rodríguez, and G. Martínez-Pinedo, *Systematic study of infrared energy corrections in truncated oscillator spaces with Gogny energy density functionals*, Phys. Rev. C **94**, 054319 (2016).
4. S. Goriely, N. Chamel, and J. M. Pearson, *Skyrme-Hartree-Fock-Bogoliubov Nuclear Mass Formulas: Crossing the 0.6 MeV Accuracy Threshold with Microscopically Deduced Pairing*, Phys. Rev. Lett. **102**, 152503 (2009).
5. M. Kortelainen, J. McDonnell, W. Nazarewicz, E. Olsen, P.-G. Reinhard, J. Sarich, N. Schunck, S. M. Wild, D. Davesne, J. Erler, and A. Pastore, *Nuclear density optimization: Shell structure*, Phys. Rev. C **89**, 054314 (2014).

6. B.G. Carlsson, J. Dobaczewski and M. Kortelainen, *Local nuclear energy density functional at next-to-next-to-next-to-leading order*, Phys. Rev. C **78**, 044326 (2008).
7. F. Raimondi, B. G. Carlsson, and J. Dobaczewski, *Effective pseudopotential for energy density functionals with higher-order derivatives*, Phys. Rev. C **83**, 054311 (2011).
8. P. Becker, D. Davesne, J. Meyer, J. Navarro and A. Pastore, *Solution of Hartree-Fock-Bogoliubov equations and fitting procedure using the N2LO Skyrme pseudopotential in spherical symmetry*, Phys. Rev. C **96**, 044330 (2017).
9. J. A. Maruhn, P.-G. Reinhard, P. D. Stevenson, and A. S. Umar, *The TDHF code Sky3D*, Comp. Phys. Comm. **185**, 2195 (2014).
10. P. Bonche, H. Flocard and P.H. Heenen, *Solution of the Skyrme HF + BCS equation on a 3D mesh*, Comp. Phys. Comm. **171**, 175 (2005).
11. W. Ryssens, *Symmetry breaking in nuclear mean-field models*, PhD Thesis, Université Libre de Bruxelles (2016).
12. W. Ryssens, V. Hellemans, M. Bender and P.-H. Heenen, *Solution of the Skyrme-HF+BCS equations on a 3D mesh, II: a new version of the EV8 code*, Comp. Phys. Comm. **187**, 75 (2015).
13. T. Matsuse, *3D-mesh Hartree-Fock calculation with finite range two-body force*, RIKEN Review **19**, 18 (1998).
14. T. Nakatsukasa *et al.*, *Stochastic generation of low-energy configurations and configuration mixing calculation*, presentation at the INT Program 13-1a, "Computational and Theoretical Advances for Exotic Isotopes in the Medium Mass Region", held at the INT Seattle, USA, March 25 - April 19, 2013.
15. H. J. Mang, B. Samadi and P. Ring, *On the solution of constrained Hartree-Fock-Bogolyubov equations*, Z. Phys. **A279**, 325 (1976).
16. J. L. Egido, J. Lessing, V. Martin and L. M. Robledo, *On the solution of the Hartree-Fock-Bogoliubov equations by the conjugate gradient method*, Nucl. Phys. **A594**, 70 (1995).
17. L. M. Robledo and G. F. Bertsch, *Application of the gradient method to Hartree-Fock-Bogoliubov theory*, Phys. Rev. C **84**, 014312 (2011).
18. E. N. E. van Dalen and H. Müther, *Triaxial deformation in nuclei with realistic NN interactions*, Phys. Rev. C **90**, 034312 (2014).
19. R. Jodon, M. Bender, K. Bennaceur and J. Meyer, *Constraining the surface properties of effective Skyrme interactions*, Phys. Rev. C **94**, 024335 (2016).
20. P. Ring and P. Schuck, *The nuclear many-body problem*, Springer Verlag (1980).
21. J. C. Pei *et al.*, *Adaptive multi-resolution 3D Hartree-Fock-Bogoliubov solver for nuclear structure*, Phys. Rev. C **90**, 024317 (2014).
22. B. Gall *et al.*, *Superdeformed rotational bands in the Mercury region: A Cranked Skyrme-Hartree-Fock-Bogoliubov study*, Z. Phys. A **348**, 183 (1994).
23. D. Baye and P.-H. Heenen, *Generalised meshes for quantum mechanical problems*, J. Phys. **A19**, 2041 (1986).
24. T. Lesinski, M. Bender, K. Bennaceur, T. Duguet and J. Meyer, *Tensor part of the Skyrme energy density functional: Spherical nuclei*, Phys. Rev. C **76**, 014312 (2007).
25. M. Bender, K. Bennaceur, T. Duguet, P.-H. Heenen, T. Lesinski and J. Meyer, *Tensor part of the Skyrme energy density functional. II. Deformation properties of magic and semi-magic nuclei*, Phys. Rev. C **80**, 064302 (2009).
26. V. Hellemans, P.-H. Heenen and M. Bender, *Tensor part of the Skyrme energy density functional. III. Time-odd terms at high spin*, Phys. Rev. C **85**, 014326 (2012).
27. S. Goriely, N. Chamel, and J. M. Pearson, *Further explorations of Skyrme-Hartree-Fock-Bogoliubov mass formulas. XII. Stiffness and stability of neutron-star matter*. Phys. Rev. C **82**, 035804 (2010).
28. J. Sadoudi, T. Duguet, J. Meyer, and M. Bender, *Skyrme functional from a three-body pseudo-potential of second order in gradients. Formalism for central terms*, Phys. Rev. C **88**, 064326 (2013).
29. J. Sadoudi, M. Bender, K. Bennaceur, D. Davesne, R. Jodon, and T. Duguet, *Skyrme pseudo-potential-based EDF parametrization for spuriousity-free MR-EDF calculations*, Phys. Scr. **T154**, 014013 (2013).
30. E. Perlińska, S. G. Rohoziński, J. Dobaczewski, and W. Nazarewicz, *Local density approximation for proton-neutron pairing correlations: Formalism* Phys. Rev. C **69**, 014316 (2004).
31. W. Ryssens and M. Bender, *Implementation of N2LO functionals*, in preparation.
32. P. Pulay, *Convergence acceleration of iterative sequences. The case of SCF iteration.*, Chem. Phys. Lett. **73**, 393 (1980).
33. Y. Zhou, J. R. Chelikowsky and Y. Saad, *Chebyshev-filtered subspace iteration method free of sparse diagonalisation for solving the Kohn-Sham equation*, J. Comp. Phys. **274**, 770 (2014).
34. M. V. Stoitsov, J. Dobaczewski, W. Nazarewicz and P. Ring, *Axially deformed solution of the Skyrme-Hartree-Fock-Bogolyubov equations using the transformed harmonic oscillator basis. The program HFBTHO (v1.66p)*, Comp. Phys. Comm. **167**, 45 (2005).
35. J. Dobaczewski and J. Dudek, *Solution of the Skyrme-Hartree-Fock equations in the Cartesian deformed harmonic oscillator basis II. The program HFODD*, Comp. Phys. Comm. **102**, 183 (1997).
36. K. Bennaceur, LENTEUR HFB Code, unpublished.
37. C. Rigollet, P. Bonche, H. Flocard, and P.-H. Heenen, *Microscopic study of the properties of identical bands in the A = 150 mass region*, Phys. Rev. C **59**, 3120 (1999).
38. M. Bender, K. Rutz, P.-G. Reinhard, and J. A. Maruhn, *Pairing gaps from nuclear mean-field models*, Eur. Phys. J. **A8**, 59 (2008) .
39. Y. Saad, *Numerical methods for large eigenvalue problems: Revised Edition*, Society for Industrial and Applied Mathematics, Philadelphia (2011).
40. W. H. Press, B. P. Flannery, S. A. Teukolsky and W. T. Vetterling, *Numerical Recipes: the art of scientific computing*, Second Edition, Cambridge University Press, Cambridge (1992).
41. K. T. R. Davies, H. Flocard, S. Krieger and M. S. Weiss, *Application of the imaginary time step method to the solution of the static Hartree-Fock problem*, Nucl. Phys. A **342**, 111 (1980).
42. P.-G. Reinhard and R. Y. Cusson, *A comparative study of Hartree-Fock iteration techniques*, Nucl. Phys. A **378**, 418 (1982).
43. G. Goh, *Why Momentum Really Works*, Distill, 2017.
44. N. Qian, *On the momentum term in gradient descent learning algorithms*, Neural Networks **12**, 145-151 (1999).
45. B. T. Polyak, *Some methods of speeding up the convergence of iteration methods*, USSR Computational Mathematics and Mathematical Physics, **4**, 1 (1964).

46. Y. Nesterov, *Introductory lectures on convex optimisation*, Springer Verlag US, Boston (2004).
47. C. K. Gan, P. D. Haynes and M.C. Payne, *Preconditioned conjugate gradient method for the sparse generalized eigenvalue problem in electronic structure calculations*, *Comp. Phys. Comm.* **134**, 33 (2001).
48. P. Bader, S. Blanes and F. Casas, *Solving the Schrödinger eigenvalue problem by the imaginary time propagation technique using splitting methods with complex coefficients*, *J. Chem. Phys.* **139**, 124117 (2013).
49. R. Car and M. Parrinello, *Unified Approach for Molecular Dynamics and Density-Functional Theory*, *Phys. Rev. Lett.* **55**, 2471 (1985).
50. J. Hutter, *Car-Parrinello Dynamics*, *WIREs Comput. Mol. Sci.* **2**, 604 (2012).
51. L. Lin and C. Yang, *Elliptic Preconditioner for Accelerating the Self-Consistent Field Iteration in Kohn-Sham Density Functional Theory*, *SIAM J. Sci. Comput.* **35**, S277 (2012).
52. V. Hellemans *et al.*, *Spurious finite-size instabilities in nuclear energy density functionals*, *Phys. Rev. C* **88**, 064323 (2013).
53. T. Lesinski, K. Bennaceur, T. Duguet, J. Meyer, *Isvector splitting of nucleon effective masses, ab initio benchmarks and extended stability criteria for Skyrme energy functionals*, *Phys. Rev. C* **74**, 044315 (2006).
54. A. Pastore, D. Davesne, and J. Navarro, *Linear response of homogeneous nuclear matter with energy density functionals*, *Phys. Rep.* **563**, 1 (2015).
55. M. Martini, A. De Pace, and K. Bennaceur, *Spurious finite-size instabilities of a new Gogny interaction suitable for astrophysical applications*, preprint arXiv:1806.02080.
56. G. Gonzalez-Boquera, M. Centenelles, X. Viñas and L. M. Robledo, *Comment on the manuscript 1806.02080v1 entitled 'Spurious finite-size instabilities of a new Gogny interaction suitable for astrophysical applications'*, preprint arXiv:1807.10159
57. M. Kortelainen, T. Lesinski, J. Moré, W. Nazarewicz, J. Sarich, N. Schunck, M. V. Stoitsov, and S. Wild, *Nuclear energy density optimization*, *Phys. Rev. C* **82**, 024313 (2010).
58. M. Kortelainen, J. McDonnell, W. Nazarewicz, P.-G. Reinhard, J. Sarich, N. Schunck, M. V. Stoitsov, and S. M. Wild, *Nuclear energy density optimization: Large deformations*, *Phys. Rev. C* **85**, 024304 (2012).
59. G. P. Kerker, *Efficient iteration scheme for self-consistent pseudopotential calculations*, *Phys. Rev. B* **23**, 3082 (1981).
60. V. Blum, G. Lauritsch, J. A. Maruhn, and P.-G. Reinhard, *Comparison of coordinate-space techniques in nuclear mean-field calculations*, *J. Comput. Phys.* **100**, 364 (1992).
61. A. Baran *et al.*, *Broyden's method in nuclear structure calculations*, *Phys. Rev. C* **78**, 014318 (2008).
62. P. Pulay, *Improved SCF convergence acceleration*, *Jour. Comp. Chem.* **3**, 556 (1982).
63. K. N. Kudin, G. E. Scuseria and E. Cancès, *A black-box self-consistent field convergence algorithm: One step closer*, *Jour. Chem. Phys.* **116**, 8255 (2002).
64. W. Ryssens, M. Bender, K. Bennaceur, J. Meyer and P.-H. Heenen, *The impact of the surface energy coefficient on the deformation properties of atomic nuclei as predicted by Skyrme energy density functionals*, *Phys. Rev. C* **99**, 044315 (2019).
65. W. Ryssens, M. Bender and P.-H. Heenen, In preparation.
66. P. Bonche, H. Flocard, and P.-H. Heenen, *Self-consistent calculation of nuclear rotations: The complete yrast line of ^{24}Mg* , *Nucl. Phys. A* **467**, 115 (1987).
67. J. Terasaki, P.-H. Heenen, H. Flocard, P. Bonche, *3D solution of Hartree-Fock-Bogoliubov equations for drip-line nuclei*, *Nucl. Phys.* **A600**, 371 (1996).
68. N. Schunck *et al.*, *Solution of the Skyrme-Hartree-Fock-Bogolyubov equations in the Cartesian deformed harmonic-oscillator basis.: (VII) hfodd (v2.49t): A new version of the program*, *Comp. Phys. Comm.* **183**, 166 (2012).